Gas-Phase Near-Edge X-Ray Absorption Fine Structure (NEXAFS) Spectroscopy of Nanoparticles, Biopolymers, and Ionic Species

8

Aleksandar R. Milosavljević, Alexandre Giuliani, and Christophe Nicolas

Contents

A.R. Milosavljević (✉)
Institute of Physics Belgrade, University of Belgrade, Belgrade, Serbia
e-mail: vraz@ipb.ac.rs

A. Giuliani
Synchrotron SOLEIL, L'Orme des Merisiers, Gif-sur-Yvette, France

UAR1008, CEPIA, INRA, Nantes, France
e-mail: alexandre.giuliani@synchrotron-soleil.fr

C. Nicolas
Synchrotron SOLEIL, L'Orme des Merisiers, Gif-sur-Yvette, France
e-mail: christophe.nicolas@synchrotron-soleil.fr

C.S.S.R. Kumar (ed.), *X-ray and Neutron Techniques for Nanomaterials Characterization*, DOI 10.1007/978-3-662-48606-1_8

1 Definition of the Topic

Near-edge X-ray absorption fine structure (NEXAFS) spectroscopy probes directly or indirectly the photoabsorption cross section of a system under study as a function of the photon energy around the core–shell ionization thresholds. When the photon energy matches the difference between the core level and an unoccupied valence level, the photoabsorption cross section increases. The core levels are associated with particular atoms within the system under the study; therefore, NEXAFS spectroscopy appears to be a very sensitive probe of physicochemical and structural properties of molecules and materials. It has been intensively applied to investigate gaseous, liquid, and solid species. In this chapter, we describe methods to perform *gas-phase* NEXAFS spectroscopy of large systems, such as nanoparticles, clusters, and biopolymers, as well as of ionic species. We also review recent research findings.

2 Overview

The development of third-generation synchrotron radiation (SR) sources, providing extremely bright and energy-resolved X-ray beams, established NEXAFS spectroscopy as a powerful and widely used technique to investigate electronic and structural properties of both organic and inorganic samples of increasing complexity. Particularly, gas-phase NEXAFS studies allow for an investigation of well-defined targets prepared under desired conditions.

Unfortunately, gas-phase NEXAFS spectroscopy of large species such as biopolymers (e.g., proteins and DNA) and nanoparticles, as well as ionic species, is experimentally very challenging due to great difficulties in both bringing large molecules or particles intact into the gas phase and providing high-enough target density, photon flux, and interaction time needed to distinguish K-shell excitation processes. Only recently, the development of new experimental techniques has allowed performing gas-phase NEXAFS of nanoparticles, biopolymers, and ionic species.

Herein, we present the basic principles of NEXAFS spectroscopy and describe the state-of-the-art experimental approaches that allow for NEXAFS spectroscopy of large biopolymers and nanoparticles isolated in the gas phase. Finally, we present some key research finding spanning from relatively small biomolecules to large biopolymers and nanoparticles.

3 Introduction

NEXAFS spectroscopy has been used to study systems of increasing complexity, from small isolated molecules to large biological objects and materials; and it has been successfully applied to gaseous, liquid, thin-layer, nanoscopic, and solid targets. There is a substantial literature on the subject, from comprehensive graduate-level textbooks presenting both the fundamental principles and the

applications of NEXAFS spectroscopy (e.g., [1]) to more specialized reviews that deal with, for example, the application of the technique in studying thin organic films and liquids [2] or DNA components [3]. Herein, the focus is on recently developed NEXAFS action spectroscopy of ionic targets as well as large species such as nanoparticles and biopolymers isolated in vacuo.

The strength of inner-shell spectroscopic techniques is based on the excitation of core-level electrons providing a highly localized nature of the triggering process and, thus, sensitive and selective probe of the electronic, chemical, and structural properties of the system [4]. With this aim, NEXAFS spectroscopy of thin molecular films has been used in recent years to investigate properties of large biologically important molecules, such as proteins, for example [5–9]. However, spectroscopic study of solid or aqueous samples may be limited in cases where intrinsic electronic and structural information is to be measured without interferences from the environment. Moreover, condensed matter samples may suffer severe radiation damage from the energetic X-ray radiation, which, in turn, may affect the results (see [10] and references therein). Gas-phase spectroscopy, on the other hand, allows studying isolated system in vacuo under well-defined conditions. Furthermore, a constant sample renewal practically prevents any radiation damage effects. Nevertheless, the crucial issue here is the kind of objects that can be transferred and isolated in vacuo with a high-enough density for inner-shell spectroscopy to be efficiently conducted.

There are tremendous amounts of results from gas-phase NEXAFS spectroscopy, which has been routinely performed on relatively small targets that can be easily brought into the gas phase. This incredible rise of the X-ray-based spectroscopy is dominantly due to the increasing number of new-generation bright SR sources. However, gas-phase X-ray spectroscopy of large targets has been reported only recently, after development of modern methods allowing for bringing such large species into the gas phase. For example, one way to obtain an intact protein in the gas phase and to submit it to X-rays is to use the electrospray ionization (ESI) [11], where protonated or deprotonated protein ions are extracted into the gas phase directly from the solution. Nevertheless, since the ionic target density is too low to measure the photon beam attenuation, NEXAFS spectroscopy must be performed as an action spectroscopy, by indirectly recording processes resulting from the X-ray absorption. A very efficient action spectroscopy is based on tandem mass spectrometry (MS^2). With the advent of modern ionization techniques, MS^2 has become one of the most powerful tools to probe the structure of biopolymers [12]. In MS^2 a desired ionic compound is isolated, activated, and mass analyzed. NEXAFS MS^2 is, therefore, based on recording the tandem mass spectra produced upon photon activation of the precursor ions, as a function of the photon energy scanned around the core ionization edge. Figure 8.1 schematically presents soft X-ray absorption processes, leading to the formation of a core hole triggering either resonant or normal Auger decays and resulting in ejection of Auger electrons and ionization of the precursor, which, finally, can be detected by mass spectrometry (see Sect. 4.2.4 for more details).

The principles of SR sources are described in Sect. 4.1. The common spectroscopic techniques are presented and shortly described in Sect. 4.2. The sources of

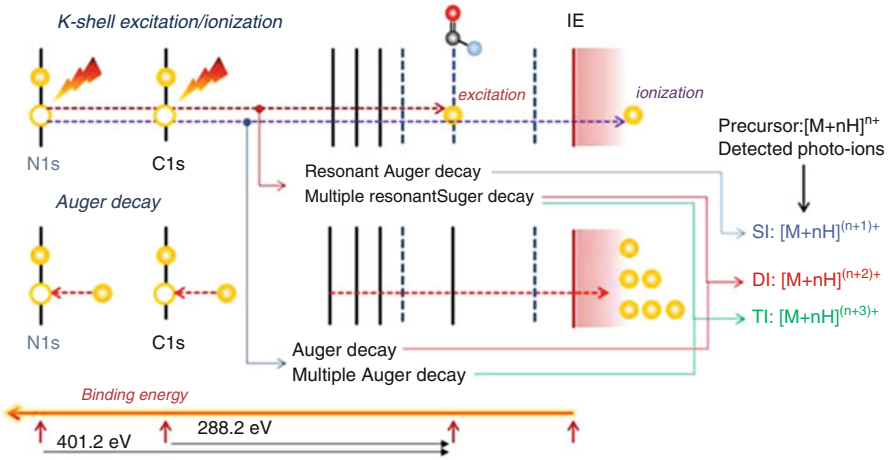

Fig. 8.1 Schematic representation of the X-ray K-shell excitation/ionization of a multiply protonated protein ion, followed by Auger decays and production of ionized cations that are detected in the experiment (Adopted from Milosavljević et al. [13])

gas-phase targets are described in Sect. 4.3. Typical experimental setups for coupling the sources of large gas-phase targets with the synchrotron X-ray beam are the subject of Sect. 4. Finally, key research findings are reviewed in Sect. 5.

4 Experimental and Instrumental Methodology

4.1 X-Ray Sources

4.1.1 Synchrotron Radiation Facilities

There are many different ways to produce X-ray photons, from laboratory X-ray tubes to the latest generation of synchrotron radiation storage rings and free-electron lasers. In this chapter, we will concentrate on accelerator-based sources. Synchrotron radiation (SR) is an electromagnetic radiation produced by the acceleration of charged particles of relativistic velocities. SR is intimately connected to a high-energy particle accelerator. Indeed, SR is the main mechanism of energy lost by the accelerated particles, due to photon emissions all along their trajectories. Ivanenko and Pommeranchuck in 1944 [14] and independently Schwinger in 1946 [15, 16] have reported the theory of SR for circular particle accelerators. SR has been observed for the first time in 1946 at the General Electric synchrotron in the United States. However, due to the complexity of the accelerator technologies and also to the dedication of these machines primarily to high-energy physics, it was only in the 1960s that SR was used for the first time for spectroscopic studies [17–20]. Thereafter, storage rings started to be progressively dedicated to SR studies, and due to the specific properties of SR light, synchrotron facilities have become one of the most

useful sources of spectroscopic studies in the twentieth century. Kuntz et al. [21] give a good overview of the early stages of SR development but also the basis of synchrotron radiation theory. The important properties of SR are:

1. A wide wavelength coverage, from THz to hard X-rays. Moreover, with the advent of the third-generation installations (see below), SR radiation can be optimized over a given energy range (vacuum ultraviolet, soft X-rays, hard X-rays).
2. A high brilliance, due to the high collimation of the emitted radiation.
3. The time structure of the pulsed light.
4. An adjustable polarization, from classic linear polarization with the electric vector parallel to the orbit plan (classic bend magnet radiation) to various polarizations including circular or elliptical (by using an insertion device such as an undulator; see below).

Figure 8.2 depicts a typical third-generation synchrotron storage ring, such as SOLEIL, the latest French synchrotron facility. The electron bunches are created by an electron gun and then first accelerated in the LINAC (linear accelerator) up to 100 MeV. Then, they are brought to the nominal energy of the storage ring in the booster ring (2.75 GeV, in the case of SOLEIL). When they reach this final energy, they are injected into the storage ring, which is composed of a succession of straight sections connected by bending magnets. Compared to second-generation installations, which use exclusively the bending magnets to produce SR radiation, the third generations use magnetic insertion devices such as undulators or wigglers [22–24], made with a periodic structure of dipole magnets. In this case, the electron bunches experience a periodic magnetic field that radially accelerates them several times, giving them an oscillatory trajectory and thus producing SR. This radiation is orders of magnitudes higher than the one produced by a standard bending magnet. Moreover, by adjusting the design parameters of the insertion device, the emission can be optimized in a narrower region around the photon energy of interest [25]. As an example, a brilliance of 10^{15} photons/s 0.1 % bw mm^2 $mrad^2$ can be achieved in the soft X-ray regime, thanks to insertion devices, such as the Apple II. These kinds of photon fluxes have made possible new studies on low-density samples under vacuum by different spectroscopic techniques and will be discussed below.

With the forthcoming generation of storage rings, the ultimate storage ring light sources [26], the diffraction limit of the machine electron optics should be achieved. With the decrease in the horizontal emittances thus reached, an additional gain of several orders of magnitude in brilliance is expected compared to existing light sources, and therefore new studies on gas-phase isolated biomolecules, clusters, and nanoparticles, which are particularly photon demanding, should be boosted. In particular, pump–probe experiments involving optical lasers would be facilitated.

In parallel with the development of synchrotron light sources, another type of installation based on the same technology is developing. Free-electron laser (FEL) sources use a linear accelerator followed by one or more undulators in series, in which the electron bunches are dumped after they emit their SR pulse. Initially used

Fig. 8.2 Schematic drawing of a third-generation synchrotron machine (SOLEIL synchrotron, France)

in the IR or in the VUV and EUV ranges, in the last decade, the X-ray FELs made available high-intensity femtosecond X-ray pulses of coherent SR to the user's community. The brilliance of FELs are orders of magnitudes higher than existing or future storage rings. As an example, the LCLS installation is capable of reaching an average brilliance of 10^{22} photon/s 0.1 % bw mm^2 $mrad^2$. These X-ray pulses are:

- Ultra-intense
- Coherent
- Ultrashort
- Having a high spatial resolution

These properties have made possible single-shot diffraction experiments of labile objects such as biomolecules or membrane proteins [27, 28] but also of nanoscale objects such as viruses [29–31] or soot particles [32]. The possibility of coupling diffraction techniques (structural information) with spectroscopic or spectrometric techniques is very promising.

4.1.2 Soft X-Ray Beamlines

SR, after being emitted by an undulator or a bending magnet, is collected tangentially to the storage ring into a beamline, which comprises a set of optical and mechanical devices used to transport, select the photon energy, and focalize the monochromatic light to the desired area in the experimental chamber. The new-generation synchrotrons can host more than 20 beamlines, each one specializing in specific scientific fields. We will concentrate in this chapter only on the soft X-ray beamlines opened to users and that are specialized in dilute matter studies. Presently, there are 16 soft X-ray beamlines of this type around the world. With the

later-generation beamlines, the synchrotron beam can be focused into a spot with dimensions of around a few hundred micrometers; even focusing to a few tens of micrometers can now be easily achieved. Also, the geometric dimensions of these synchrotron beams at the focal point are now matching the dimension of nanoparticle beams (few hundreds of micrometers) or even liquid microjet beams (tens of micrometers). Moreover, the brilliance on the sample can reach 10^{13} photon/s mm^2 0.1 % bw mrad^2. The resolving powers of the photon beam have also increased. Nowadays, a beamline designed for high resolution can reach a maximum resolving power of 100 000.

4.2 General Techniques

4.2.1 X-Ray Absorption Spectroscopy

NEXAFS spectroscopy is a commonly used technique in gas phase or surface science experiments [1]. A core electron is excited to an unoccupied molecular orbital or to the continuum, and then a de-excitation occurs, via Auger decay or fluorescence, to fill the core hole created. In the soft X-ray regime and with low Z-elements, the fluorescent channel remains weak. Usually in NEXAFS spectroscopy, spectra exhibit π^* or σ^* resonances when the energy difference between the core level and one unoccupied molecular orbital equals the photon energy. Additionally, Rydberg series converging toward the K-edge ionization threshold may also be observed for isolated species. Thus, information about the electronic structure may be obtained from such experiments. Moreover, with NEXAFS spectroscopy, specific bonds such as C–C, C=C, C=O, etc., can be identified. It is important to note that the position of the σ^* resonances compared to the absorption onset has been related to the bond length [33–35]. The simplest way to measure NEXAFS spectra is to record total ion or electron yields as a function of the photon energy. A basic setup consists of two polarizable grids that attract the cations (or the electrons, depending on the chosen mode), a multichannel plate chevron stack, and a 50 Ω adapted full metal anode.

The absorption of a photon just below or just above the core ionization threshold promotes a molecule to an energetic core-excited state that dominantly relaxes via Auger decay [10, 36, 37]. Below the threshold, the core electron is promoted to an unoccupied molecular orbital, triggering the resonant Auger decay or an X-ray fluorescence process [37], leading mostly to a single-ionization process (an Auger electron emission) [10] but also a multiple ionization. When the photon energy is above the core ionization threshold, the core electron is ejected directly into the ionization continuum, and the system may relax via a normal Auger decay, producing a multiply charged ion (emission of both a core ejected and Auger electron(s)). In all cases, X-ray absorption produces ionized species that can be detected by means of mass spectrometry methods (see Fig. 8.3). Fine-tuning of the photon energy over the resonant excitation energies and the core ionization threshold may result in a drastic change in the fragment ion yields, since the intensive ionization/fragmentation is actually triggered by the resonant photon absorption or the ionization.

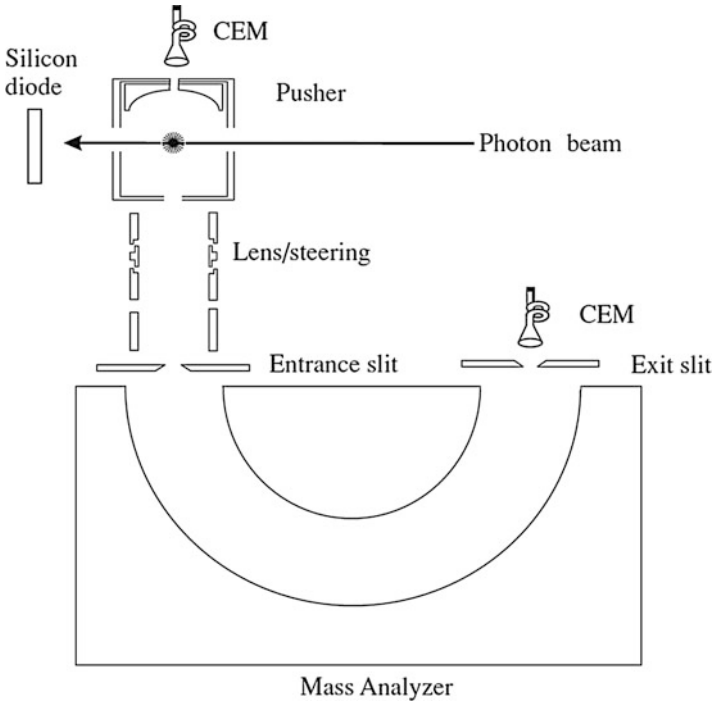

Fig. 8.3 Schematic representation of the experimental setup used for the partial-ion-yield measurements (Reprinted from Guillemin et al. [38]. © IOP Publishing. Reproduced with permission. All rights reserved)

In the case of relatively small gaseous molecules, X-ray absorption generally leads to an intensive fragmentation of the target. Therefore, the results represent partial-ion-yield curves of selected fragments, possessing rich spectroscopic structure below the ionization threshold corresponding to the excitation energies of the target molecule. Also, doubly charged fragment ions have increased yield above the ionization threshold. The application of X-ray absorption mass spectrometry has been limited until recently only to relatively small molecules, owing to difficulties to place in gas-phase large species such as neutral biomolecules (see the Introduction and the following section about sources of gas-phase targets).

4.2.2 X-Ray Photoemission Spectroscopy

With NEXAFS spectroscopy, there is no analysis of the kinetic energy (E_{Kin}) of the electron detected. Indeed, the absorption cross section is a sum over all the electrons ejected belonging to shells with a binding energy (E_{BD}) lower than or equal to the photon energy (E_{Photon}). In photoemission experiments, the kinetic energy of the electron is analyzed. The relation between the kinetic energy (E_{Kin}) of the emitted electron and the binding energy (E_{BD}) is given by Eq. 8.1:

$$E_{Kin} = E_{Photon} - E_{BD} \tag{8.1}$$

Various kinds of spectrometers have been developed in order to analyze the kinetic energy of the emitted electrons [39, 40]. Either the time of flight of the electron is measured and its correspondent kinetic energy is calculated or energy-dispersive elements (electrodes) are used to deflect the electrons according to their kinetic energy. In this last case, an electron lens system is needed to collect, transport, and focus the photoelectrons on the entrance slit of the analyzer. Information on the electronic structure of matter can be obtained through measurement of the electron binding energies and their chemical shifts [41]. Atoms and molecules [42, 43], clusters [44–50] or nanoparticles, and bulk material [51–56] are investigated with this technique. As shown by Eq. 8.1, for a given electronic state, increasing the energy of the incoming photon will increase the kinetic energy of the emitted electron. Moreover, according to the universal inelastic mean free path curve of an electron, the surface sensitivity can be tuned. This is an important point, as it explains the extreme surface sensitivity of nanoparticle studies in the soft X-ray regime (see Sect. 5.3).

4.2.3 Coincident Measurements

Compared to conventional electron spectroscopy, an electron–electron or electron–ion coincidence measurement is always much more powerful in providing a direct view of the interaction processes [57–62]. Different experimental setups are used with soft X-ray synchrotron radiation [60, 63–65]. One of the key points in such a measurement requires that both electrons and ions are collected and detected as efficiently as possible, hence to maximize coincidence efficiency. Fragmentation of gas-phase molecules [62] or small biomolecules (see Sect. 4.1), clusters [66, 67], condensed matter [68–71], and nanoparticles [52] has been investigated with this technique.

4.2.4 X-Ray Action Spectroscopy of Trapped Ions

Recently, the use of ion-trapping devices has attracted a growing interest, as it allows performing mass and charge-selected spectroscopy [72]. These experiments are sequential in nature. Ions of interest are generated in a variety of ion sources (described in Sect. 4.3.3), which may be pulsed (such as laser desorption) or continuous (such as electrospray ionization). The ions are then selected and stored in an appropriate ion trap. When the storage capacity of the trap is reached, X-ray beam from a beamline is admitted to the trap and irradiates the ions for a controlled amount of time. After the interactions, the ion trap is emptied, and its content analyzed. The whole sequence is described in Fig. 8.4.

The steps described in Fig. 8.4 may be repeated several times until satisfactory statistic is reached before the photon energy is changed and the cycle is reiterated.

The ion spectroscopy experiments belong to the class of action spectroscopy, in which specific photophysical or photochemical reaction giving a detectable product ion is used to derive partial yields over the photon energy range of interest [10, 73, 74] (see Fig. 8.5). Thus, monitoring each particular process as a function of the

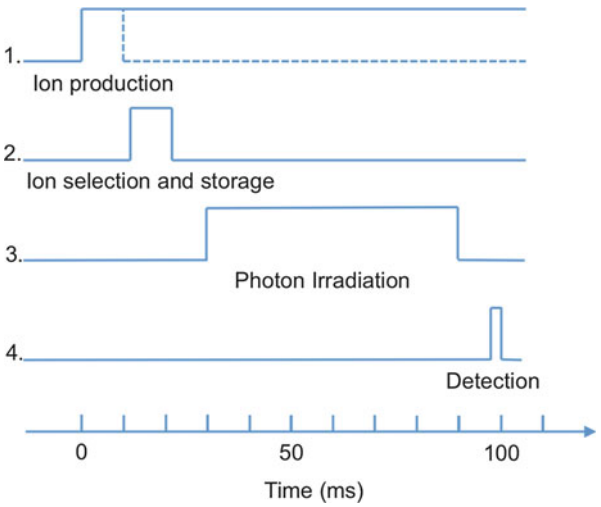

Fig. 8.4 The typical time frame of an ion trap-based experiment. Ion production may be either pulsed (as depicted by the *dashed lines*) or continuous (*solid line*)

photon energy offers the possibility to selectively study molecular core-level processes. Nevertheless, great care should be taken to avoid sequential two-photon reactions, in which photoproducts absorb a photon and react. Usually, the yields of photoproducts are maintained low enough for these sequential reactions to be negligible. When the photon energy is scanned over the K-edges, in analogy with NEXAFS spectroscopy, the technique has been referred to by a group as near-edge X-ray absorption mass spectrometry (NEXAMS) [73].

4.3 Sources of Gas-Phase Targets and Their Coupling with X-Ray Beam

4.3.1 Neutral Molecules

Relatively small molecules and biomolecules, existing as liquids or solids at room temperature and possessing low vapor pressure, are commonly vaporized into the gas phase and introduced into the vacuum conditions using ovens. The design of the oven must ensure, on the one hand, an increased vapor pressure needed to produce a satisfactory high intensity of the molecular beam, and on the other hand, it must prevent overheating and thermal decomposition of the molecules. In the case of crossed-beam experiments, the oven design also needs to ensure the formation of a geometrically well-defined target molecular beam. More details about the design of the ovens can be found in a number of previous publications and books (e.g., see [75] and references therein).

Experiments using ovens should be carefully performed when thermally fragile targets are investigated, such as some amino acids or oligosaccharides, for example. Still, with a fine regulation of the temperature, this approach may have some advantages over other soft-evaporation techniques. For example, Touboul

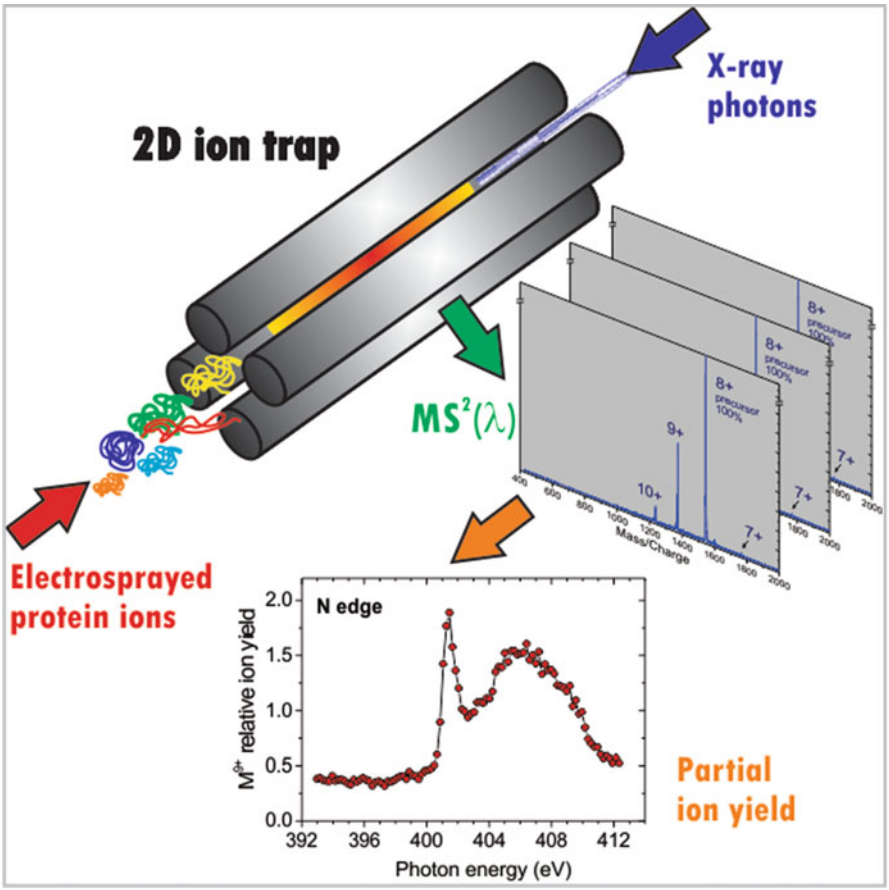

Fig. 8.5 Schematic representation of the near-edge X-ray absorption tandem mass spectrometry experimental method using a linear ion trap fitted with an ESI source (Reprinted with permission from Milosavljević et al., The Journal of Physical Chemistry Letters (2012) 3, 1191 [10]. Copyright (2012) American Chemical Society)

et al. [76] have recently investigated VUV photoionization of gas-phase amino acids adenine and cytosine. In this work, the authors have compared two different techniques to obtain intact gas-phase amino acids, namely, a temperature-controlled oven placed under vacuum and an aerosol setup coupled to a thermodesorber module (see section "Aerosol Technique Used for Neutral Biomolecule Production"). They concluded that although the aerosol thermodesorption allowed for lower sample consumption while still providing a satisfactory sensitivity, it resulted on relatively lower overall experimental energy resolution in comparison with the oven vaporization followed by beam expansion, due to the higher internal energy deposited on the neutral target molecules. It should be noted, however, that the same authors [76] suggested that the aerosol thermodesorption technique could be improved and be

more suitable for large and thermolabile neutral biological compounds (nucleotides, oligopeptides, polysaccharides, etc.).

4.3.2 Nanoparticles and Large/Fragile Neutral Biomolecules and Clusters

Laser Ablation

One way to isolate nanoparticles or clusters is to produce them directly under the vacuum. For example, a pulsed laser may be focused on a rotating target sample comprising a rod or disk of the material under study, which is placed in front of a molecular beam nozzle where a carrier gas is expanding [77]. This expansion is either free or confined in a channel (from a few millimeters in diameter to over a centimeter long) in order to reach a higher average of the cluster size distribution. Nanoparticles with a diameter of a few nanometers can be generated. The beam is then skimmed before entering the spectrometer chamber. However, to obtain sufficient energy per pulse, mostly nanosecond or picosecond low repetition rate lasers (from 10 to 1000 Hz) are used. The very unfavorable duty cycle (the SR is usually pulsed around few hundred of MHz) may account for small number of studies using this technique with SR [78].

Aerosol Techniques

There are different kinds of nanoparticle generators (atomizers, vibrating orifices, etc.), each one with their specificity and optimized for a certain type of nanoparticle. Some are able to disperse directly nanoparticle powders, while others produce liquid droplets containing nanoparticles, such as those developed to study aerosols.

Usually, the nanoparticle sample is diluted in water or alcoholic solution. The solution is sprayed at the atmospheric pressure via an atomizer into small droplets, which contain the nanoparticles. The atomization is based on the Venturi effect, where a high-velocity gas (usually air with a pressure of 1–2 bar expanding through a diaphragm of few hundred microns) sucks the solution through a capillary placed orthogonally to the gas flow. The liquid is then transformed into small droplets under the action of the high-velocity jet. This generator is well suited to nanoparticles with a diameter of 10–2000 nm. Densities of particles from 10^6 up to 10^8 particles/cm^3 can be reached. It is the most commonly used method in synchrotron studies owing to its continuous mode of generation, but also because constant particle size distribution is generated. One drawback is the relatively high quantity of nanoparticles needed for an experiment. Indeed, concentrations around 1 g/L are usually required, which prevent from using of nanoparticles that cannot be produced in high quantity or those with a high cost. To remove the solvent, the aerosols pass through diffusion dryers, made of a stainless steel mesh tube surrounded by silica gels. After solvent removal, the dried nanoparticle beam is sent to the aerodynamic lens (see section "Aerosol Technique Used for Neutral Biomolecule Production", Fig. 8.6) to be focused under vacuum. The aerosol distribution exiting an atomizer is polydisperse in size.

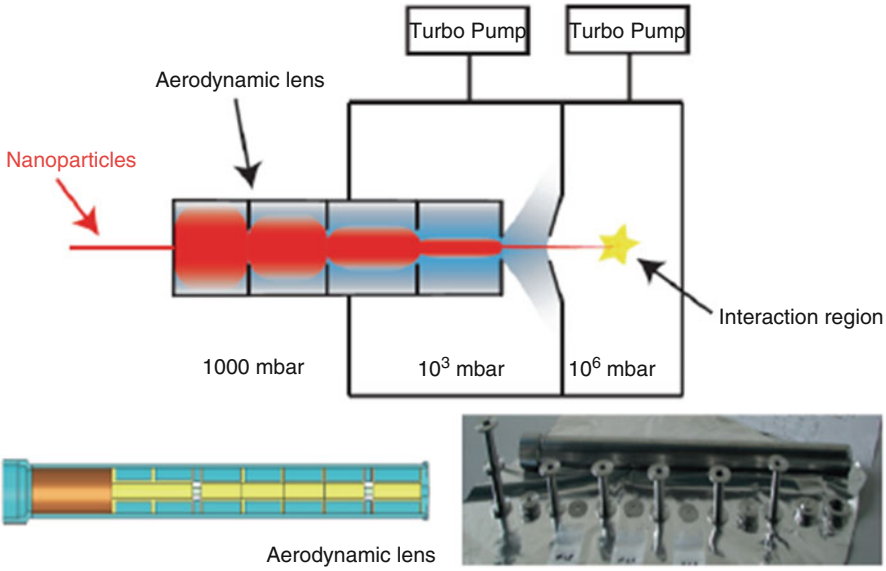

Fig. 8.6 *Top*: schematic drawing of an aerodynamic lens to focus a nanoparticle beam under vacuum. *Bottom*: details of the current aerodynamic lens used by PLEIADES beamline [79] and a picture of the easily interchangeable apertures and spacers that allow quick switching between different lens geometries

For smaller-sized nanoparticles, from 2 to 100 nm, an electrospray source (see section "Aerosol Technique Used for Neutral Biomolecule Production") followed by an ionizer (radioactive source or X-ray lamp) can be used. In this case the suspension of nanoparticles with a buffer is pushed through a capillary. The electric field applied to the capillary tip creates a Taylor cone producing small droplets. A sheath flow of CO_2 and air transports the droplets to a chamber, where their high number of charges created by electrospray ionization will be reduced by the ionizer source. The sheath flow participates also in the evaporation of the solvent. At the end, a very narrow size distribution of nanoparticles (almost monodispersed) can be reached, with a density of up to 10^7 particles/cm^3. The liquid consumption compares favorably to that required for an atomizer source. However, this type of source has not been used often in a synchrotron facility. This is probably because only a ^{210}Po ionization source was available when those experiments started, which leads to difficulties due to nuclear safety regulations. This problem was recently solved by the possibility of using an X-ray lamp as an ionizer. However, as will be discussed in section "Aerosol Technique Used for Neutral Biomolecule Production", the difficulty of focusing under vacuum nanoparticles with a diameter smaller than 30 nm represents a major limitation in the use of the electrospray as a conventional nanoparticle source for soft X-ray synchrotron studies.

Aerosol Technique Used for Neutral Biomolecule Production

Kevin et al. [80] demonstrated for the first time that an aerosol technique could be used to produce under vacuum fragile neutral biomolecules in order to be studied by SR. The biomolecule is simply dissolved into a solution (1.5 g/L), which is sprayed with an atomizer. After passing through the diffusion dryer, the aerosol of bio-nanoparticle has a size distribution centered on 280 nm. After being focused under vacuum by an aerodynamic lens (Fig. 8.6), the nanoparticle beam impacts a hot tip placed a few millimeters from the synchrotron beam, in the spectrometer chamber. The hot tip is usually a rod of a few millimeters in diameter and made from copper or porous tungsten (for better efficiency of vaporization). A proportional–integral–derivative controller drives a heater cartridge to adjust and stabilize the temperature. The bio-nanoparticles, impacting the hot tip, are flash vaporized and create an almost continuous plume of neutral, intact biomolecules, if the temperature of the hot tip is properly chosen. Peptides, polypeptides (such as gramicidin), fragile organic molecules, and beta-carotene have been produced [76, 80–83]. One drawback of this technique is the perturbation induced by the hot tip on the pulsed high-voltage fields applied to the mass spectrometers to extract the photoions, inducing a loss in its resolution. If only mass spectrometry is required, decoupling the position of the ion created by the SR and the ion's mass spectrometer acceleration region has solved this problem [84]. Flash vaporization of bio-nanoparticles has been used only with VUV SR as an ionization source. An attempt to use this technique with the soft X-ray photon was tried at PLEIADES beamline (see Fig. 8.7). A reflectron time-of-flight spectrometer was used to detect any ions coming from the ionization of the neutral parent molecule. If it was still possible to detect ion signals for photon energy up to 100 eV (corresponding to the maximum photon flux of the beamline), measurements around the different K-edges were not successful. This is probably due to the difference in ionization cross sections between valence electrons and core electrons. Also, it seems that the density of neutral molecules created by this technique is insufficient to be able to run experiments that include electron spectroscopy or coincidence measurement.

Coupling Nanoparticle Sources to X-Ray Beam

The development, by McMurry and coworkers [85–88], of aerodynamic lens systems built from a succession of orifices with decreasing diameters along the stream flow marked an important milestone in the possibility of focusing particles under vacuum. Indeed, the submillimeter-sized particle beams created this way are intense, due to the high transmission efficiency of the lens over a wide range of NP diameters (30–1000 nm), and collimated, which make them particularly compatible with under vacuum diagnostic techniques such as mass spectrometry or photoelectron spectroscopy.

In brief, an aerosol source (see Sect. 4.3.2) transfers into gas phase, from the atmospheric pressure, NPs mixed with a carrier gas (air, N_2, He, Ar, etc.). After passing through a diffusion dryer, the aerosol obtained is directed by a split flow

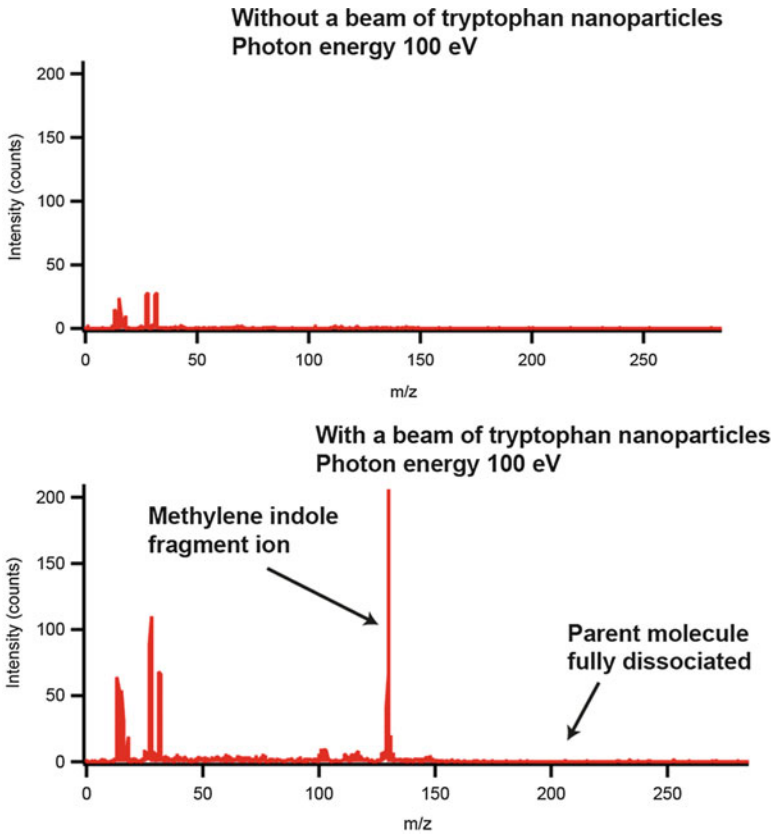

Fig. 8.7 Signal of tryptophan obtained at 100 eV at the PLEIADES beamline by the technique of flash vaporization of bio-nanoparticles. *Left*: without nanoparticle beam. *Right*: when the particles impact the hot tip. At this high photon energy, the parent molecule is completely dissociated

device into three different flows: one going to the aerodynamic lens system, one to a granulometry analyzer for characterization of the nanoparticles' concentration and size distribution, and one toward a gas exhaust line to equilibrate the gas flow. The gas–particle mixture enters the aerodynamic lens via the critical orifice (or chocked inlet orifice), a calibrated hole of around 200 μm, followed by a relaxation chamber. Its role is to fix the mass flow rate into the system and to reduce the ambient pressure to the operating pressure of the lens system. Focusing is accomplished by successive compression and expansion of a carrier gas through the series of coaxial orifices (thin plates) with different diameters (in the millimeter range). The NPs are progressively separated from the gas streamlines, due to the inertia principle, and focused along the lens symmetry axis. After exiting the accelerating nozzle of the lens into a differentially pumped chamber, the collimated nanoparticle beam passes through a skimmer

to reach the interaction region inside the spectrometer chamber. The skimmer, in this case, does not skim the nanoparticle beam, but has a role of limitation of conductance to assure that the pressure in the spectrometer does not exceed 10^{-5} mbar. The nanoparticle beam, focused with the aerodynamic lens, provides a continuously renewed sample. Charging effects, or degradation of the sample via interaction with energetic radiation, cannot happen in this case. Figure 8.6 shows a principle drawing of a typical aerodynamic lens arrangement and a dismounted lens from [79].

The aerodynamic lens is able to focus nanoparticles into a beam of diameters < 500 μm (FWHM). The beam is also highly collimated (sometimes less than 1 mrad). Different types of aerodynamic lenses exist, which have been experimentally [86, 87, 89–92] or theoretically [85, 88, 93–95] characterized. Theoretical simulations are complex and therefore are mainly limited to spherical nanoparticles, quite often far from the real object under study, considering, for example, soot or agglomerated particles. One important parameter is the Stokes number, which describes a particle's behavior in fluid flow when they are meeting an obstacle, such as the element of an aerodynamic lens. This dimensionless number is a ratio between the characteristic of the particle and the characteristic of the obstacle. It can be express as the ratio between the kinetic energy of the nanoparticle and the dissipated energy due to the friction forces with the fluid. If the Stokes number is equal to zero, the particles will follow perfectly the fluid flow, but if the Stokes number is much bigger than one, the particles are not influenced by the fluid flow and they can impact either the diaphragm or the inner part of the lens and be lost. In reference [85], different trajectories of an identical set of particles are presented, but with different Stokes numbers. The best focalization is achieved with a Stokes number equal to one. In order to test new geometries of lenses, Wang and McMurry developed an "aerodynamic lens calculator" simulation software, where the geometry of the lens can be defined, as well as the different conditions of operation (carrier gas properties, nanoparticle properties, and lens conditions) [91].

Each set of orifices with different diameters will be able to focus different sizes of particles. Ideally, by stacking a sufficient number of orifices, an aerodynamic lens should be able to focus a wide range of nanoparticles. The lens geometries cited above are able to focus and have transmission efficiencies close to 100 % for particles with diameters above 30 nm. Below 30 nm, the Brownian motion of the nanoparticles starts to play a non-negligible role and tends to defocus the beam inside the lens, but also after the nozzle, which degrades the density and collimation of the created beam. Being able to create an intense beam of nanoparticles with a diameter below 10 nm is of crucial importance, since size and quantum effects start to be present only in particles close to nanometer size [52, 96]. It is important to note that most of the first calculations on a particle's trajectories inside the aerodynamic lens did not take into account diffusion effects [85, 86, 88]; this has been corrected by newest studies [94, 95, 97]. However, it is possible to find lenses that have been designed especially for focusing particles to below 30 nm [93, 98–100]. Another approach, concerning charged nanoparticles, is to use the radio-frequency ions guide technique to store and concentrate the nanoparticle at the SR interaction region

before their analysis. Various kinds of nanoparticles have been studied with this technique, which is more complex than a simple aerodynamic lens but does not have a size limitation [101–104]. Also, different synchrotron radiation-based experimental setups with an aerodynamic lens system can be found [52, 79, 82, 84, 105].

4.3.3 Ionic Species

Today, the variety of ion sources available is very important, with new developments appearing regularly and giving easier access to new classes of molecules. A typical ion source comprises a desorption/desolvation method to place the species of interest in the gas phase, and an ionization means to produce charged species. It is, however, possible to categorize ion sources into two main classes: atmospheric pressure ionization (API) sources and vacuum sources.

Sources functioning under reduced pressure include electron impact ionization of vapor gas phase, as used by Thissen and coworkers [106]. This method, which may be either pulsed or continuous, is applicable to gases and to sample with a sufficient vapor pressure. Electron beam ion trap (EBIT) sources create highly charged ions at rest by passing high current density electrons into drift tubes in which ions are confined by magnetic and electrical fields [107]. An EBIT source has been used by Epp and coworkers to perform soft X-ray spectroscopy on trapped highly charged ions [108]. Lau and coworkers have used magnetron sputtering by argon atoms of targeted metallic species to produce intense beams of neutral and ions [109]. Gas-phase aggregation is achieved in a volume cooled by liquid nitrogen and leads to an abundant cluster production. Owing to the relatively high flow of gases, the source has to be vigorously differentially pumped by high-capacity turbomolecular pumps. Laser vaporization has also been successfully used to produce intense cluster ion beams [110] suitable for spectroscopy at FLASH [50].

API sources are newcomers in this field and are based on the generation of ions at atmospheric pressure prior to their introduction into the vacuum through an orifice or a capillary differentially pumped. These ion sources have been successfully used by Giuliani and coworkers [72] and by Schlathölter and coworkers [73, 111]. Both of these groups have taken profit from the capabilities of electrospray ionization (ESI) to place in the gas-phase variety of molecules and clusters [112]. The mechanism of ESI has been a subject of considerable study [11, 113]. In ESI, a solution containing a molecule of interest at concentrations of 10^{-4} to 10^{-6} mol/L is pushed through a stainless steel needle at flow rates typically in the 1–20 μL/min. The needle is polarized at 3–5 kV with respect to the sampling orifice of the mass spectrometer. In combination with ion funnels, high ionization and transmission efficiencies can be reached for electrosprayed ions [114]. Nanospray ionization, a variation on the theme of electrospray, has drastically reduced consumption of matter, as flow rates in the nanoliters per minute are required.

Other API ion sources appear particularly interesting, although they have not been used for ion spectroscopy purposes. Atmospheric pressure photoionization (APPI) is a method giving access to very hydrophobic compounds [115] and has proven its potential in ionization of polycyclic hydrocarbons and fullerenes [116].

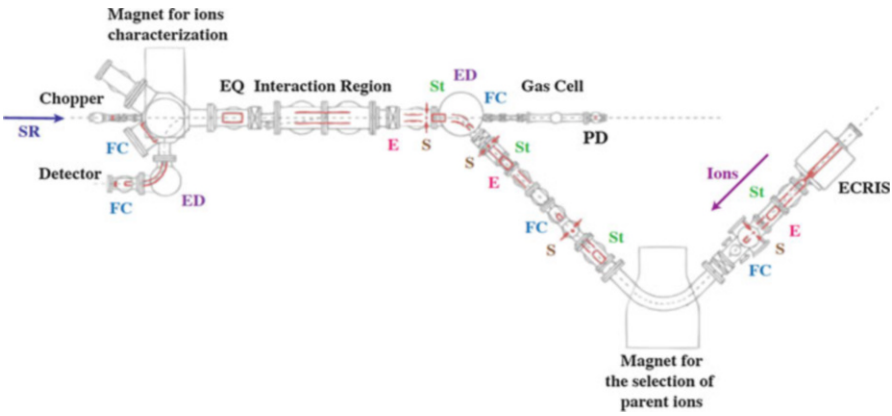

Fig. 8.8 Scheme of the MAIA merged-beam experimental setup on the PLEIADES beamline. The ion optics used for the ion beam transport are represented in *red*. *ECRIS* electron cyclotron ion source, *E* einzel lens, *St* set of horizontal and vertical steerers, *S* collimating slits, *FC* Faraday cup, *ED* electrostatic deflector, *IR* interaction region, *EQ* electrostatic quadrupole, *SR* synchrotron radiation, *PD* photodiode (Figure graciously provided by Jean-Marc Bizau, Orsay)

Coupling the Ion Sources with the X-Ray Beam

The main difficulty encountered when performing mass-selected ion spectroscopy lies in the confinement of high-enough quantity of ion in a precise region of space where the interaction with the incident X-ray photon beam will take place. Photon sources of high brilliance are required for this kind of spectroscopy, such as delivered by SR sources and FELs. Three different kinds of experimental arrangements have been combined with SR and FELs to perform X-ray spectroscopy: crossed-beam, merged-beam, and ion-trapping setups.

Historically, mass and charge-resolved action spectroscopy has been achieved using the so-called merged-beam technique. This method was developed by Peart and coworkers in the 1970s for the study of electron impact processes on atomic ions [117]. Later on, the method was adapted to the study of photoionization processes using synchrotron radiation by Lyon and coworkers using the Synchrotron Radiation Source (SRS) at Daresbury, UK [118]. In merged-beam experiments, ions, produced from a plasma ion source, for example, are accelerated, selected by a magnetic mass filter, and merged over tens of centimeters with monochromatic photons from synchrotron radiation beamlines. Ion current in the 1–100 nA is produced after mass selection at keV kinetic energy. Both ion and photon beams are allowed to interact over 50 cm or more, in the μs time range [119–121]. Figure 8.8 presents a typical merged-beam setup, as found on the PLEIADES beamline at SOLEIL [122]. Fairly high target densities are obtained, but relatively elevated background is generated by collisions of the fast ions with residual background gases. The use of ion-trapping devices for X-ray spectroscopy has brought an interesting and

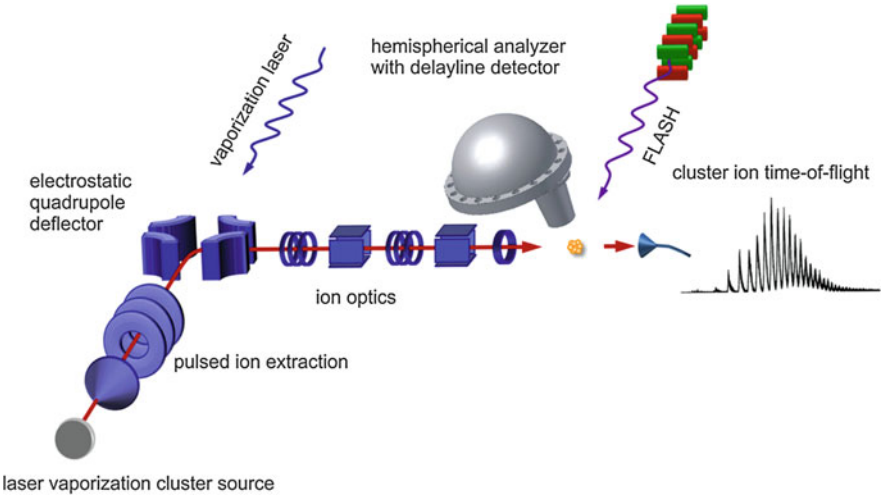

Fig. 8.9 Experimental setup for cluster ion photoelectron spectroscopy (Reprinted with permission from Bahn et al. [50]. © IOP Publishing & Deutsche Physikalische Gesellschaft. CC BY-NC-SA)

complementary alternative to merged-beam setup for atomic, cluster, and molecular ion studies [106, 121, 123].

Photoelectron spectroscopy has appeared as a subsequent development of the merged-beam setup, with the pioneering work of Bizau and coworkers at Super ACO in the 1990s in the VUV [124, 125]. However, recently crossed-beam arrangements have appeared at FLASH for photoelectron studies on anions in the VUV [126] and soft X-ray range [50]. In this kind of arrangements, ion beam is crossed with the FEL radiation from FLASH. The photoelectron distributions are measured with a hemispherical electron analyzer, as shown in Fig. 8.9, and ions are time-of-flight analyzed. By matching the ion acceleration and the delay-line detectors with the FEL pulsing frame, photoelectrons can be assigned to a specific ion mass, without upstream ion selection.

Ion traps are devices using a combination of electric and/or magnetic fields to confine charged species in vacuum. These devices, widely used in various fields of analytical mass spectrometry, have found applications in spectroscopy [72, 74, 127–129]. Several setups based on ion trapping have been used to probe ions in the X-ray regimes, using Penning traps [106, 130, 131], Paul traps [73, 111, 132] or linear ion traps [10, 109, 133].

Ion-trapping experiments complement advantageously the merged-beam techniques. First, these devices can be associated with a variety of ion sources, such as electron impact ionization in vapor phase, sputtering sources, laser desorption, or electrospray ionization. Second, ion traps compensate for a lower amount of ions in

the interaction region by longer interaction times, which may be extended up to tens of seconds. Third, ion traps may be associated with other mass analyzers in hybrid instruments, such as with time of flight or as stand-alone spectrometers. Finally, the ability to repeat *n*-times the selection and activation steps opens up the possibility to do successive tandem mass spectrometry (MS^n).

The first coupling of an ion trap with synchrotron radiation was originally reported in 1991 by Kravis and coworkers [134]. In this experiment, performed at the National Synchrotron Light Source facility in Brookhaven (USA), the authors investigated inner-shell photoionization and sequential ionization of atomic dications produced by electron impact and stored in a Penning trap. In this pioneering work, the incident radiation was not monochromatic, which complicated the analysis of the results. The first coupling of ion-trapping devices with monochromatic synchrotron radiation appeared almost simultaneously using a Penning trap at Elettra (Italy) [106] and a linear ion trap at Bessy (Helmholtz-Zentrum Berlin, Germany) [133]. In the Elettra experiment, a portable FT-ICR mass spectrometer (MICRA) was coupled to the gas-phase beamline [106]. Xenon radical cations were produced by electron impact on xenon inside the trap and were selected subsequently. Irradiation of these precursor ions with monochromatic radiation in the extreme UV proved to be possible and is compared favorably with merged-beam experiments. The MICRA mass spectrometer has very appealing capabilities. Its high mass resolving power of 73,000 may be very useful to separate signal from the background. However, FT instruments suffer from lower dynamics than ion-counting mass spectrometer, which makes detection limits around 200 ions [131]. Nevertheless, the magnetic field used in Penning trap to confine the ions has been elegantly used to perform X-ray magnetic circular dichroism using the 7 T from the Bruker APEX mass spectrometer [131]. Figure 8.10 shows the setup, which was placed 4 m downstream the U52-PGM at Bessy. Clusters were prepared by laser desorption on a rotating foils combined with adiabatically expansion under vacuum of the clusters mixed with helium. XAS measurements were performed with linear polarized radiation and XMCD with circularly polarized radiation.

Alternatively, linear ion traps offer the advantage of higher detection dynamics and higher column density, as interaction lengths up to 265 mm have been achieved [109]. In this last setup, presented in Fig. 8.11, storage and irradiation take place in a linear ion trap, and ion detection is achieved by a time of flight, giving a mass resolving power of 300 in the Wiley–McLaren configuration and 1700 in the reflectron configuration [109]. A similar coupling, based on a Paul trap and time-of-flight detection of the ions, has been coupled to VUV and soft X-ray beamline [73, 132, 135, 136].

In 2012 Milosavljevic et al. [10, 137] reported the coupling of a commercial linear ion trap with synchrotron radiation beamlines in the soft X-rays at the SOLEIL synchrotron radiation facility, as shown in Fig. 8.12. This commercial machine (LTQ XL from Thermo Finnigan) allows performing isolation, storage, irradiation, and detection using the same linear ion trap device, making the system

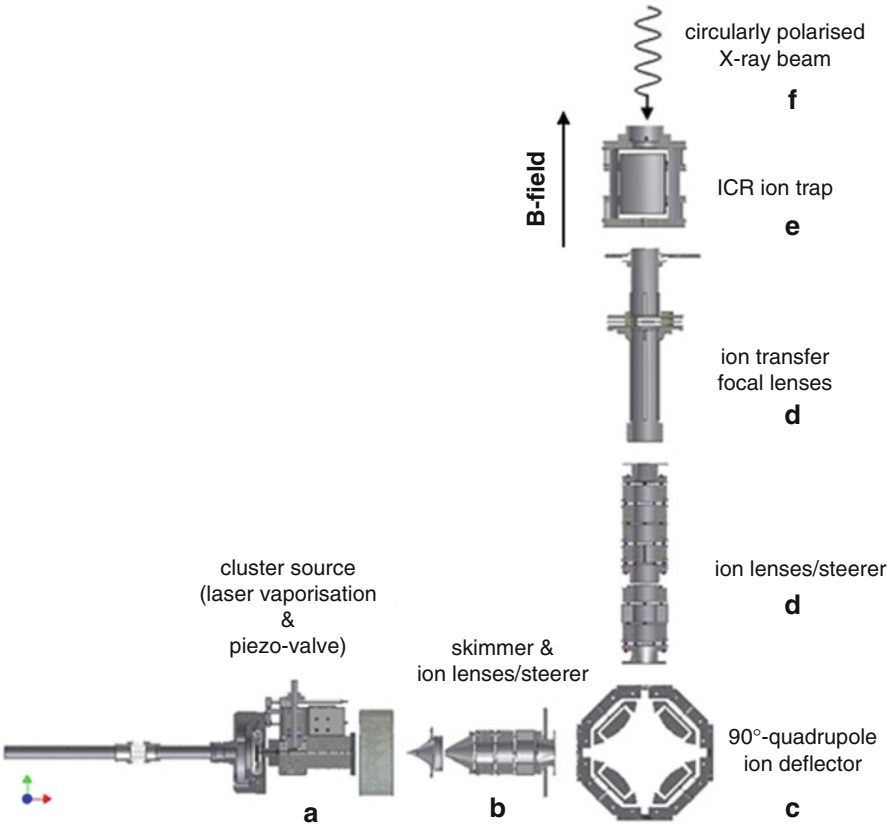

Fig. 8.10 XMCD setup based on a Bruker APEX III mass spectrometer for metal cluster X-ray spectroscopy (Reprinted from Peredkov et al. (2011) *Journal of Electron Spectroscopy and Related Phenomena*, *184*, 113 [131]. Copyright (2011), with permission from Elsevier)

very compact. The quadrupole consists of rods with a hyperbolic profile, and each rod is cut into three axial sections of 12, 37, and 12 mm length [138]. The ion trapping is achieved by a combination of DC and RF fields applied to each rod. The ion ejection is made through 0.25 mm height slots that had been cut along the middle side electrodes. The ejected ions are converted using conversion dynodes and the electron signal detected by two electron multipliers. Such ion ejection is mandatory for the irradiation of the ion packet. This mass spectrometer is able to reach a mass resolving power above 25,000 [139]. The LTQ from Thermo operates in a helium gas bath at 10^{-3} mbar inside the trap, in contrast to the other ion-trapping systems for which helium was pulsed to collisionally cool the ions. Such a permanent helium pressure in the trap has been shown to lead to minor evaporation of weakly bound clusters [112]. Another interesting feature of this

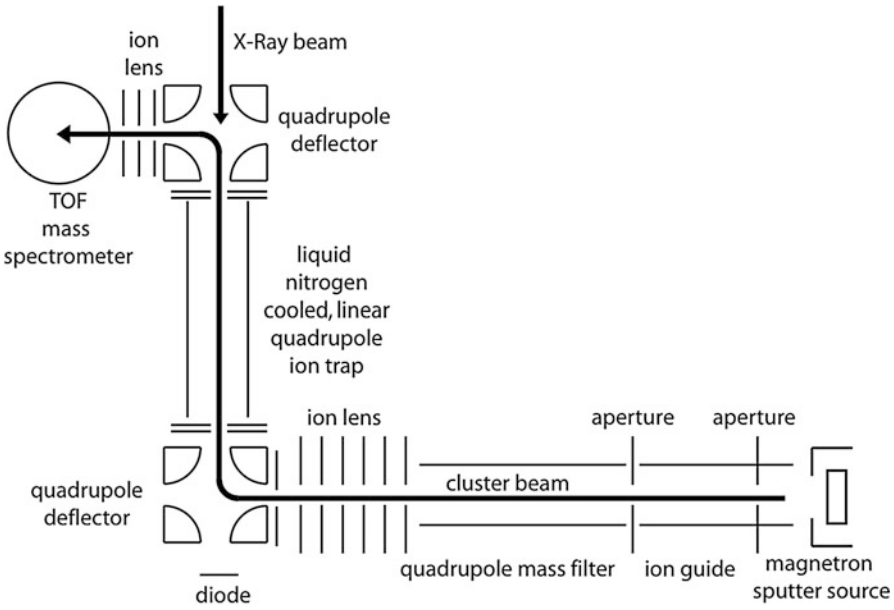

Fig. 8.11 Setup based on a linear ion trap (Reprinted from Hirsch et al. [109]. © IOP Publishing. Reproduced with permission. All rights reserved)

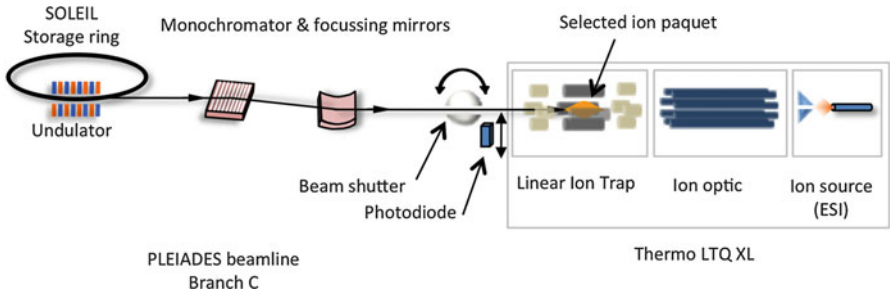

Fig. 8.12 Scheme of the coupling of a LTQ XL mass spectrometer with the soft X-ray beamline PLEIADES at SOLEIL synchrotron facility (Adapted with permission from Milosavljević et al. [137])

commercial instrument is the availability of various ion sources, such as atmospheric pressure chemical ionization (APCI), atmospheric pressure photoionization (APPI), atmospheric pressure matrix-assisted laser desorption/ionization (AP-MALDI), and electrospray ionization (ESI). Such a diversity of reliable ion sources allows accessing a variety of targets, ranging from biomolecules [140–144], weakly bound aggregates [145, 146], or clusters [112].

5 Key Research Findings

5.1 Small Biomolecules

Gas-phase NEXAFS spectroscopy of biologically relevant molecules has attracted a great deal of attention in recent years. The general idea is that gas-phase experiments of relatively small molecules under very well-defined conditions can provide a fundamental understanding of the structure and physicochemical properties of certain compounds, as well as reliable data sets on their interactions with X-ray irradiation. The latter can serve as a benchmark for theoretical modeling and, hopefully, an extrapolation of the conclusions to real biological objects, thus allowing modeling their interaction with X-rays. As an introduction to gas-phase NEXAFS spectroscopy of large vital biopolymers such as DNA/RNA and proteins, discussed in more detail later on, this subsection reviews recent results on biomolecules representing building blocks of biopolymers. These relatively small molecules such as nucleobases and amino acids can be brought into the gas phase by using simple thermal vaporization techniques (Sect. 4.3.1) and studied by inner-shell spectroscopy. We also include a short paragraph (Sect. 5.1.2) reviewing recent results on partial-ion-yield spectroscopy of small organic molecules, which is out of scope of the present work. However, the experimental technique and the characteristic ion yields are relevant to the X-ray absorption tandem mass spectrometry of large biomolecules presented in Sect. 5.5.

5.1.1 Gas-Phase X-Ray Spectroscopy of DNA Components and Amino Acids

Nucleic Acid Components

A number of studies on X-ray interaction with isolated DNA and RNA nucleobases or with some of their derivatives have been reported so far, since a beam of free nucleobases in the gas phase can be routinely formed using ovens and submitted to tunable X-ray synchrotron radiation. A more detailed review on the recent progress in the application of synchrotron-based spectroscopic techniques such as NEXAFS, for the study of nucleic acids, can be found in Wu et al. [3].

Bolognesi et al. have performed both X-ray photoemission and NEXAFS spectroscopy of pyrimidine and halogenated pyrimidines, supported by calculations [147–149]. The authors assigned and tabulated detailed N and C K-edge spectroscopic results, presenting core excitation energies obtained both from the experiment and from the calculations, for pyrimidine and substituted pyrimidines. They have shown that in fact all the carbon and nitrogen atoms in pyrimidine are affected by halogenation due to the higher electronegativity of the halogen atoms compared to substituted hydrogen. For example, a chemical shift of the π^* core excitation to higher energies at the substituted C atom due to an antiscreening effect has been observed; also, the substitution of an H atom with a larger halogen atom induces a chemical shift of the σ^* core excitation to lower energies due to an increase of the bond length [148]. Moreover, using resonant Auger electron-ion coincidence

spectroscopy, Bolognesi et al. [149] have shown that the fragmentation of pyrimidine triggered by a resonant core excitation depends only on the final state of the singly charged ion.

Comprehensive gas-phase core-level studies on other isolated nucleobases, including cytosine, uracil, and guanine, as well as their derivatives, have also been performed recently. Feyer, Plekan, and coauthors have investigated tautomerism in cytosine, uracil, guanine, 4-hydroxypyrimidine, S-methyl-2-thiouracil, and 2-thiouracil [150–154]. They have shown, for example, that population of tautomers in the gas phase can significantly vary over the nucleobases and that a substitution of hydrogen by a halogen atom can strongly influence the dominance of particular tautomer. It should be also noted that Hua et al. [155] performed first calculations of the N 1s NEXAFS spectra of the guanine and cytosine nucleobases and their tautomers in order to investigate the potential of NEXAFS analysis to study hydrogen-bond structure in DNA.

Fragmentation of DNA components following core ionization has been also investigated in the Kukk group using synchrotron radiation in combination with coincident detection of energy-resolved electrons and mass-resolved ions. They have investigated site-selective carbon core ionization of gas-phase pyrimidine derivatives [156], thymine and uracil and its derivatives [157, 158], and even thymidine [159], which is the only neutral nucleoside to be investigated by X-rays in vacuo due to its higher vapor pressure. The use of coincident spectroscopy allowed authors to resolve an intensity of specific fragmentation channels as a function of the initial core ionization site and the correlation between the ionized site and the bond breakage locations. Moreover, in the case of a more complex thymidine molecule, the authors reported a strong difference between valence and core ionization-induced fragmentation, demonstrating a specificity of X-ray interaction with biomolecules [159]. Along the same line of research, the group also investigated fragmentation of DNA and RNA sugars following C 1s and O 1s ionization [160].

Amino Acids

Gas-phase X-ray spectroscopy of amino acids has been attracting great deal of attention in recent years, since these biomolecules are still small enough to be brought into the gas phase relatively easily using classical temperature-controlled ovens, in contrast to their polymers – peptides and proteins. Recent studies include coincident X-ray spectroscopy [161–163], as well as both core-level photoemission and C, N, and O K-edge NEXAFS spectroscopy [164–167].

NEXAFS spectroscopic studies of isolated gas-phase amino acids allow for an investigation of inherent properties of these compounds, without intermolecular interactions occurring in solid or solvated samples that inevitably influence their electronic structure and physicochemical characteristics. On the other hand, gas-phase NEXAFS spectroscopy of relatively short chains of amino acids (peptides) also allows for a controlled study of the intramolecular interactions in biopolymers defining their structure and properties. For example, Feyer et al. [164] reported detailed comparison between NEXAFS spectra of isolated amino acid glycine (Gly) and a corresponding dipeptide glycylglycine (see Fig. 8.13). The

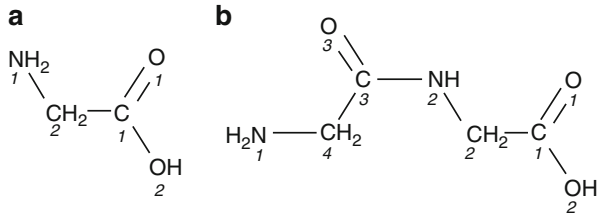

Fig. 8.13 Chemical structures of (**a**) glycine and (**b**) glycylglycine. *Italics* indicate the numbering of heavy atoms (Reprinted with permission from Feyer et al. (2009) *The journal of physical chemistry. A*, *113*, 10726 [164]. Copyright (2009) American Chemical Society)

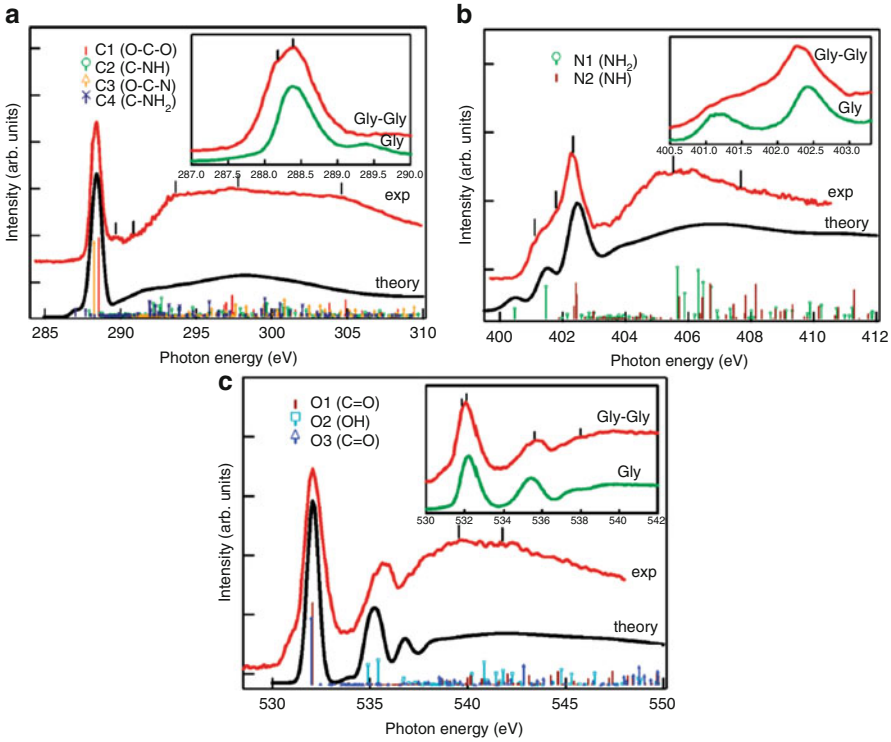

Fig. 8.14 NEXAFS of Gly-Gly compared to Gly (*insets*) for different K-edges. (Reprinted with permission from Feyer et al. (2009) *The journal of physical chemistry. A*, *113*, 10726 [164]. Copyright (2009) American Chemical Society)

later study is important as investigating the influence of polymerization of amino acids to the NEXAFS spectra. Figure 8.14 presents NEXAFS C, N, and O K-edge spectra of Gly-Gly compared to Gly [164]. The calculated transitions are also indicated in the same figure. The might of NEXAFS spectroscopy is that it is chemically sensitive – the resonant transitions associated with different C, N, and

O atoms (chemical shift) can be distinguished, which is particularly expressed in the case of the resonant transition to π^*_{CN} orbital either from N1 or N2. Moreover, the dimerization of the molecule and its three-dimensional rearrangement also affect the NEXAFS spectra, as with the internal hydrogen bonding between NH_2 and NH groups, the resonance associated with the N1 1s $\rightarrow \pi^*_{CN}$ transition shifts with respect to Gly by ~0.6 eV to a lower photon energy.

5.1.2 Partial-Ion-Yield Spectroscopy of Small Biomolecules

The absorption of a soft X-ray photon by a relatively small gaseous molecule produces a highly energetic core-excited state, which dominantly decays by a nonradiative Auger process leading to molecular ionization and intensive fragmentation due to the Coulomb repulsion [38]. Below the core ionization threshold, the resonant photon absorption thus leads to an increased fragment ion yield, allowing for NEXAFS action spectroscopy. Furthermore, the possibility to monitor the yield of a selected ionic fragment as a function of the photon energy – the partial-ion-yield spectroscopy [38, 168] – offers a number of advantages with respect to total electron or total ion yield such as investigating channels that are highly selective with respect to different types of resonances or detecting transitions otherwise hidden. This method has been applied to study very interesting phenomena but, until recently, only to small gaseous organic molecules such as formic acid [38] or phenol [169].

5.2 Clusters

Gas-phase clusters are a logical bridge between isolated species in the gas phase and bulk materials. Inner-shell spectroscopy can provide deep insight into the electronic structure of clusters thanks to its chemical specificity. The technique has proven to be a very powerful tool for gas-phase spectroscopy and surface science, but its application to clusters, either free or immobilized, is recent. For clusters, it is well known that the bulk picture is at least partially inadequate. Indeed, in clusters a large part of the atoms belong to the surface, where the electronic structure is different from the rest of the material [170]. The study of cluster properties as a function of size provides fundamental insights of importance in chemistry and physics. The first observation of metal clusters in an ion trap was made by laser vaporization [171].

5.2.1 Atomic Clusters

Gas-phase optical spectroscopy of isolated clusters is not a trivial task. Measurement of photon beam attenuation through dilute sample represents a straightforward mean of accessing optical and magneto-optical properties of isolated cluster ions. Such measurements have been reported for Mn^+ [172, 173] and silver cluster ions using cavity ring-down spectroscopy [174, 175]. However, the so-called photon-trap method is hitherto restricted to the near UV range. Using action spectroscopy, Lau and coworkers have reported the first X-ray absorption of size-selected free metal clusters [109, 133]. This group has studied a variety of mass-selected atomic cluster ions produced by a sputter-magnetron gas-aggregation source, such as titanium [133, 176], vanadium

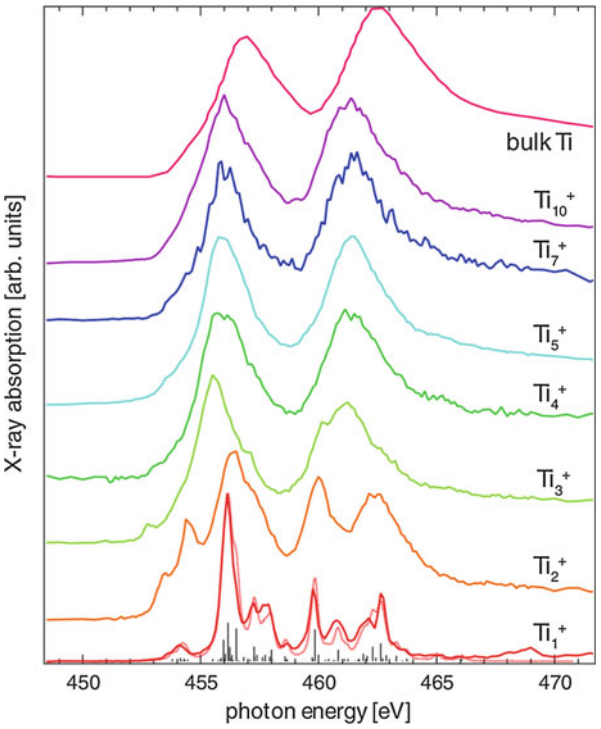

Fig. 8.15 X-ray absorption spectra of size-selected titanium species, showing the trend from isolated atomic ion to bulk titanium (Reprinted figure with permission from Lau et al., *Physical Review Letters*, 101, 153401 (2008) [133]. Copyright (2008) by the American Physical Society)

[131, 133, 176], cobalt [131, 133, 176], chromium [109, 176], manganese [176], silicon [177, 178], iron [176], nickel [179], and niobium [131]. Following X-ray photoabsorption, the mass-selected clusters may decay through emission of Auger electrons leading to multiply charged clusters, which, in turn, may further evaporate. Monitoring of the product ion abundance as a function of the photon energy provides a mean for measuring absorption spectra. X-ray action spectroscopy combined with mass and charge-selected targets has been used to derive fundamental properties and trends from the isolated atomic ion to increasing cluster size and up to the bulk. Inner-shell electron binding energy spectra and HOMO–LUMO band gap have been measured for doped silicon clusters [177]. Energy core-level shifts appear to be sensitive to the local electron density and can lead to structural assignments. A comprehensive study on metallic clusters on homonuclear 3d transition metal ranging from Ti to Ni and composed of 1–200 atoms has been carried out at the 2p X-ray absorption edge, as exemplified for titanium in Fig. 8.15.

In combination with an applied magnetic field, this powerful technique has allowed X-ray magnetic circular dichroism (XMCD) spectroscopy to be performed on mass-selected clusters [130, 131, 180–182]. The feasibility of such implementation has been demonstrated on Co_{22}^+ clusters [131]. Spin and angular momentum could be determined for Co clusters composed of 8–22 atoms as a function of the temperature [130]. The magnetism of Fe [180, 182], Co [182], and Ni [182] clusters

has been investigated as a function of the number of constituting atoms. The effect of a single impurity in silicon clusters could also be observed on magnetic moments [181].

Photoelectron spectroscopy of isolated and mass-selected metallic clusters has been recently reported using free-electron lasers, which allows compensating the low target density with increased photon fluxes within the pulse. In a pioneering study at FLASH in the VUV, the binding energy of 5d electrons of Pb cluster anions has been measured as a function of size [126]. A metal to non-metal transition has been evidenced, in agreement with previous theoretical calculations. Further refinement of the electron spectrometer has allowed accessing higher photon energy in the soft X-ray regime at 263.5 eV in Pb anionic clusters [50]. In contrast to valence-shell ionization, inner-shell ionization produces a short-lived highly excited neutral. This technique might provide information about the different relaxation dynamics of valence and core-level holes.

5.2.2 Molecular Clusters

The fine structure of X-ray absorption spectra provides unique insights into the electronic structure of molecular systems; core electron binding energies are particularly sensitive to the local chemical environments (chemical shift). Efforts in X-ray action spectroscopy of ionic clusters have been focused on atomic clusters, and we are not aware of any studies of this kind for molecular clusters. Ryding et al. [112] have studied ammonium bisulfate clusters at oxygen and nitrogen 1s and at the sulfur 2p edges, as shown in Fig. 8.16, and at selected stoichiometries, using the commercial linear ion trap system coupled to the PLEIADES beamline at the SOLEIL facility (described in Sect. 4.3). In this work, careful analysis has allowed identifying X-ray-induced dissociation (XRID) from collisionally activated dissociation. The ion trap used in this work operates at relatively high helium pressure. Interestingly, XRID leads to loss of several constituting units from the clusters. The effect of photoelectrons produced by helium photoionization has been investigated and shown to be negligible. This preliminary work has paved the way for the establishment of action spectroscopy on mass-selected clusters as a general-purpose method for detailed structural analysis of small molecular clusters. These species are of interest in atmospheric chemistry for nucleation processes and represent model systems for hydrogen bonds and intramolecular protolysis.

Daly and coworkers [183] have used ESI to produce silver-based nanoclusters in the gas phase and studied the optical properties of this material using the SOLEIL device coupled to a VUV beamline. Studies in the X-ray range of these clusters are very likely to develop in a near future.

5.3 Nanoparticles

Nowadays, nanotechnologies are widespread in our daily lives. This has become possible because even though syntheses of nanoparticles are complex, they can still

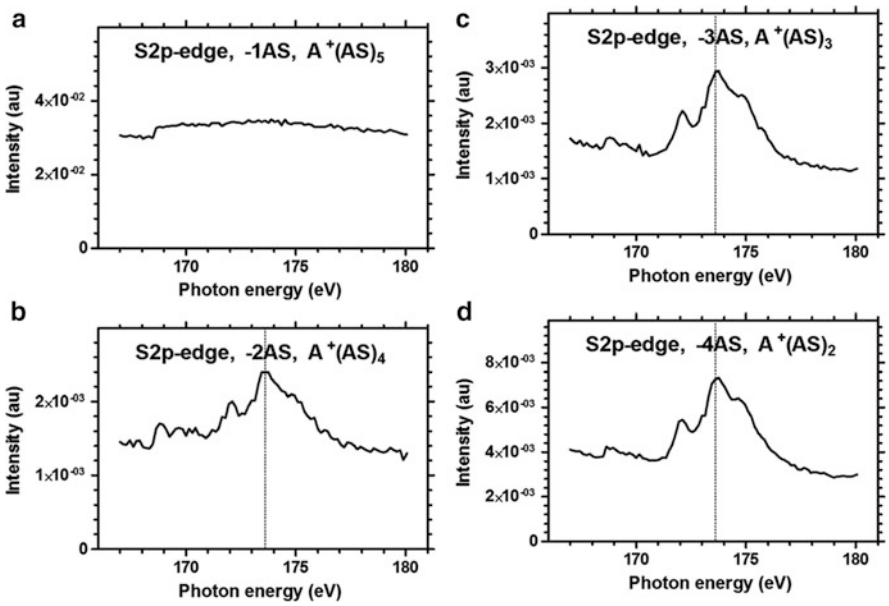

Fig. 8.16 Soft X-ray spectra for losses of increasing number of monomers from ammonium sulfate $A(AS)_6^+$ cluster around the sulfur 2p-edge (Reprinted with permission from Ryding et al. [112]. Published by The Royal Society of Chemistry)

be transposed into mass production units. The final size and composition of nanoparticles can be well tailored by their production processes, whether colloidal or polymer chemistry [184, 185] or laser pyrolysis [186, 187] is used. Thus, using the aerosols techniques to transfer them into gas phase does not need further size selection, assuming that no agglomeration process is present in the solution.

As discussed above, one of the main benefits of studying free nanoparticles is the avoidance of the influence of a substrate on their physical and chemical properties. An additional reason is the possibility of running in situ measurements of nanomaterials which can, for example, easily react with oxygen. A striking example is given by the recent study on pre-fullerenic nanoparticles by Ravagnan et al. [188]. This NEXAFS spectroscopy study on free carbon nanoparticles generated by a pulsed microplasma source clearly demonstrated, for the first time, the presence of distinct sp hybridization resonance [78]. It may sound surprising that only two recent studies in which special care was taken to avoid sample oxidation, either by in situ measurement [189] or by transporting the sample under vacuum [190], claimed the eventual presence of two distinct sp and sp^2 hybridization resonances. By varying the time between the detection of electron and the discharge in the plasma source, for which the NP size and structure evolve, Ravagnan et al. demonstrated that the relative amount of sp and sp^2 bonds varies all along the growth of the NPs. This discovery may have an important impact in fields such as astrochemistry or combustion.

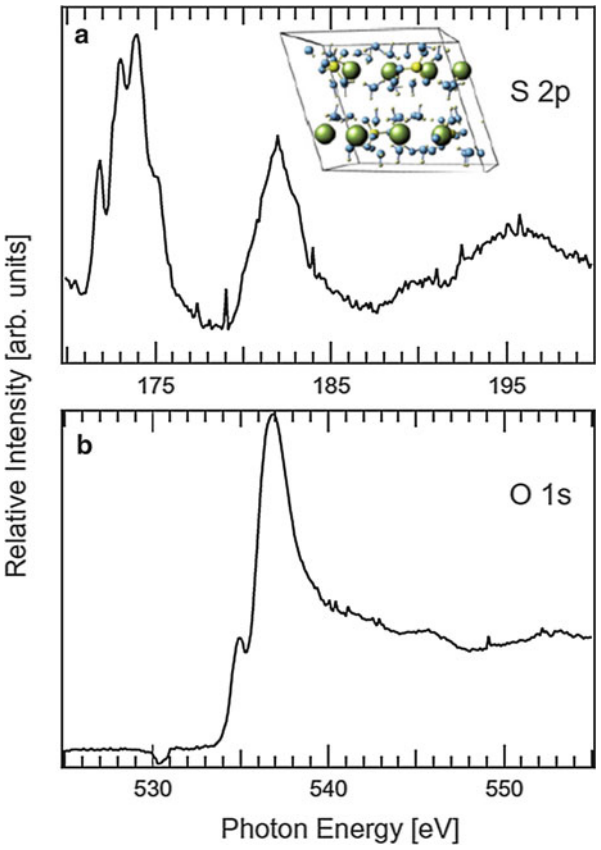

Fig. 8.17 Total electron yields from freestanding sodium sulfate nanoparticles, which present a Glauber's salt structure (given in *inset*) for Na_2SO_4 (Reprinted from Antonsson et al. (2013) *Chemical Physics Letters*, *559*, 1 [52]. Copyright (2013), with permission from Elsevier)

A detailed review of free nanoparticles studied by soft X-ray synchrotron radiation is given by Antonsson et al. [52], gathering all the studies done before 2013. We will concentrate on the two studies of near-edge spectroscopy reported by the authors.

The first study is on solid nanoparticles produced from a sprayed aqueous solution of sodium sulfate. When drying, the droplets give rise to Glauber's salts: $Na_2SO_4.10H_2O$. This example highlights the ability of near-edge absorption spectroscopy in probing the local electronic structure of the absorbing atom. Indeed, if the near-edge spectra of the sodium sulfate taken at the S 2p-edge (see Fig. 8.17) display an identical structure to that obtained for the dry sodium sulfate [191], a shift in photon energy of around 0.8 eV toward the higher photon energy is observed for the Glauber's salt structure. This could indicate a difference in the local chemical environment of the absorbing sulfur atom between the dry and wet sample. Moreover, there exists a difference in shape of the feature at 181 eV, assigned to the S 2p → d shape resonance [192]. In the absorption spectra at the O 1s-edge, features associated with bound oxygen in the sulfate group, as well as in crystalline water, are present, but signatures of liquid water are also visible. All these findings are in favor

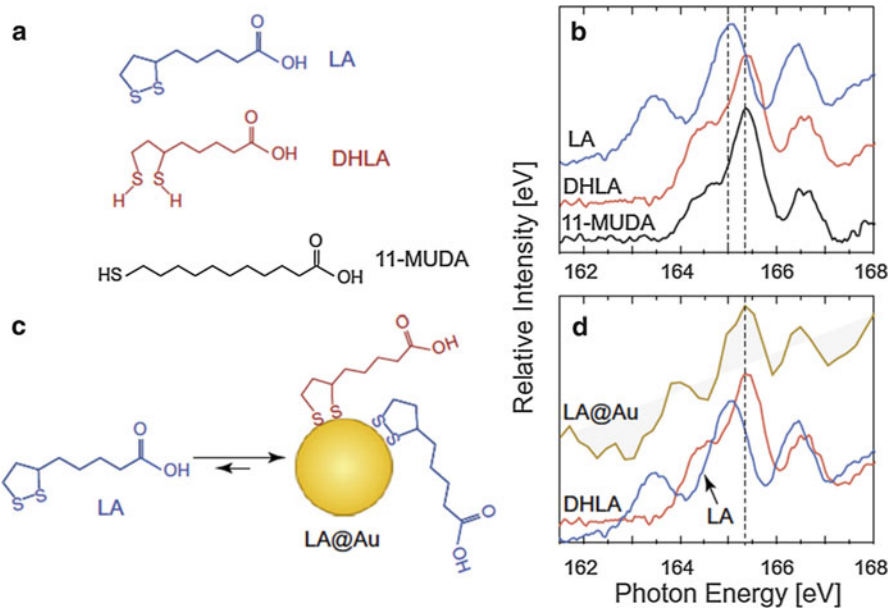

Fig. 8.18 Near-edge absorption spectra at the S 2p-edge, for (**b**) pure ligand nanoparticles (see *text*) and for (**d**) functionalized gold nanoparticles with lipoic acid (LA), according to the schematic reaction depicted in (**c**) (Reprinted from Antonsson et al. (2013) *Chemical Physics Letters*, *559*, 1 [52]. Copyright (2013), with permission from Elsevier)

of a higher number of water molecules than in pure Glauber's salts. In addition, they do not bind exclusively within the crystal water. Bonds with the sulfate group may also exist, which induce the energy shift observed in the near-edge spectrum at the S 2p-edge. A very interesting point raised by the authors is that NaCl nanoparticles, prepared in the same way, do not display strong evidence of water inclusion [193]. Also, the in situ preparation of nanoparticles, by an atomization of a solution, still conserves some of the properties of the solute.

The second study focuses on functionalized gold nanoparticles with mono- or divalent thiol ligands and, more precisely, on how the ligands bind to the 47 nm +/− 10 nm gold nanoparticles. This work is in line with previous S 1s-edge NEXAFS and XPS studies that demonstrate that dihydrolipoic acid is bonding with both sulfur sites to gold nanoparticles [194, 195]. First, the absorption spectra of pure ligand nanoparticles were recorded (see Fig. 8.18 a and b) for comparison to spectra obtained with free functionalized gold nanoparticles (see Fig. 8.18 c and d). Three different thiols were selected for this study: lipoic acid (LA), dihydrolipoic acid (DHLA), and 11-mercaptoundecanoic acid (11-MUDA). All the features for the pure ligand nanoparticle spectra are in accordance with the previous work of Dezarnaud et al. [196]. The peak at 163.3 eV corresponds to the S $2p_{3/2} \rightarrow \sigma^*$ (S–S) transition, which is why it can be observed only in the LA spectrum, and the most intense feature of all the different spectra corresponds to a superposition of the S $2p_{1/2} \rightarrow \sigma^*$

(C–S) and S $2p_{1/2} \rightarrow \sigma^*$ (C–S) transition. Even if the signal from the functionalized nanoparticle (LA@Au) is lower than the pure ligand nanoparticle signal due to a low density of ligand bound to the gold nanoparticles, interesting features in the spectra can be seen. The authors report slight shifts of 0.15 eV and 0.30 eV toward higher photon energies for 11-MUDA@Au and LA@Au, respectively, indicating chemical bonding between the ligands and the nanoparticles. Moreover, the reaming feature assigned to S 2p3/2 → sigma* (S–S), with a relative intensity identical to the one obtained with pure nanoparticles of LA, indicates that the S–S distance remains constant when lipoic acid is bound to the gold nanoparticle. With deeper analysis of the spectrum, the authors estimate that DHLA ligand could be present up to 20 %. With this study, the authors demonstrate that LA binds mostly as dithiolane to gold nanoparticles, which is in agreement with previous studies made with other spectroscopic techniques [197, 198].

In these two examples, the authors demonstrated the possibilities and the sensitivity of near-edge absorption spectroscopy when free nanoparticles are coupled with soft x-ray radiation. The element and the surface selectivity of the soft X-ray regime, coupled with near-edge absorption or photoemission studies, could play an important role in improving knowledge of the physical chemistry occurring at the surface of the nanoparticles. Even if the number of these studies to date remains still marginal, in the framework of nanomaterial studies, it should increase rapidly, as dedicated source and end stations are now available for users in several synchrotrons [47, 52, 79, 82, 84, 101].

5.4 Small Ions

In their pioneer work, Kravis and coworkers have investigated photoionization of dication of argon [134] and xenon [199] stored in a Penning trap. The doubly charged precursor ions were formed by electron impact ionization of neutral gas in the trap, stored, and photoionized by a broadband synchrotron radiation beam (white beam) from a bending magnet. The distribution of photoion charge states following K-shell photoionization could be measured and showed abundant sequential photoionization as a function of the irradiation time. This technique has the potential of producing highly charged ions.

The first reports of monochromatic photoionization on atomic ions were produced in parallel by Lau and coworkers on transition metal at Bessy synchrotron [133] and by Thissen and coworkers on xenon radical ion at Elettra synchrotron (Trieste) [106]. These studies have been extended to krypton ion at SOLEIL synchrotron [121, 123], as well as 3d elements such as calcium and copper at Bessy synchrotron [179]. Ion trap experiments showed the potential to offer control on the initial state of the target ion, allowing photoionization studies on either electronic ground state or on metastable species. This specificity complements nicely previous merged-beam experiment, in which the use of electron cyclone resonance sources produces a manifold of excited species [121, 200].

5.5 Biopolymer Ions

NEXAFS spectroscopy of large isolated gaseous biopolymer ions such as peptides, proteins, and DNA has become possible only recently with development of ion trap-based experiments (see Sect. 4). The method consists of coupling an ion trap with brilliant third-generation soft X-ray synchrotron sources, allowing to reach both a sufficient target density and preservation of the ion packet for a sufficient time (for more details and an extended reference list on the coupling of an ion trap mass spectrometer with a synchrotron photon beam, see a recent review article by Giuliani et al. [72]). Large biopolymers are introduced into the gas phase by use of modern ionization techniques such as electrospray ionization (ESI) (see Sect. 4).

Ion traps allow performing tandem mass spectrometry at the *n*th level. Therefore, the NEXAFS spectroscopy of a particular precursor is actually performed as an action spectroscopy, by collecting tandem mass spectra as a function of the activation photon energy (see Sect. 4.2.4).

The results represent a number of tandem mass spectra recorded as a function of the photon energy scanned over C, N, or O K-edge in small steps. The NEXAFS partial ion yields are finally obtained after normalization to the total ion current and the photon flux.

Two experimental setups coupling ion traps with SR have been developed more or less at the same time (see [72] for more details): Schlathölter and coworkers have developed a setup that couples a Paul ion trap with the SR and using a time-of-flight (ToF) analysis of the ionic products [135], and Giuliani and coworkers have developed a setup based upon coupling of a linear quadrupole ion trap mass spectrometer ("Thermo Scientific LTQ XL"), equipped with ESI and nano-ESI probes, with SR [143, 144]. In this section, we review recent results from NEXAFS action spectroscopy of large biopolymer ions, namely, peptides, proteins, oligonucleotides, and polycyclic aromatic hydrocarbons (PAHs).

5.5.1 Peptides

González-Magaña and coauthors have reported a pioneering study on the dissociation of the gas-phase protonated peptide leucine-enkephalin (Leu-Enk) $[YGGFL + H]^+$ ion upon soft X-ray absorption in the vicinity of the C K-edge [73]. The experiment has been performed by coupling a Paul ion trap with a SR beamline and by recording tandem mass spectra as a function of the X-ray energy. From the MS^2 spectra both the total photoabsorption yield and the partial ion yields of specific fragments have been extracted and discussed. The authors named the technique as near-edge X-ray absorption mass spectrometry (NEXAMS), since it corresponds to NEXAFS spectrometry performed on condensed phase targets. Except that NEXAMS is performed on gas-phase species, the advantage of incorporating the mass spectrometry into the method allows the study of resonant core excitations and core ionizations with respect to fragment specificity, i.e., specific bond breaking (see Fig. 8.19). The authors could distinguish specific electronic transitions, such as C 1s $\rightarrow \pi^*$ excitations in aromatics at 284.4 eV or C 1s $\rightarrow \pi^*_{C=O}$ transitions corresponding to amide group along the peptide backbone at 288.4 eV. They could

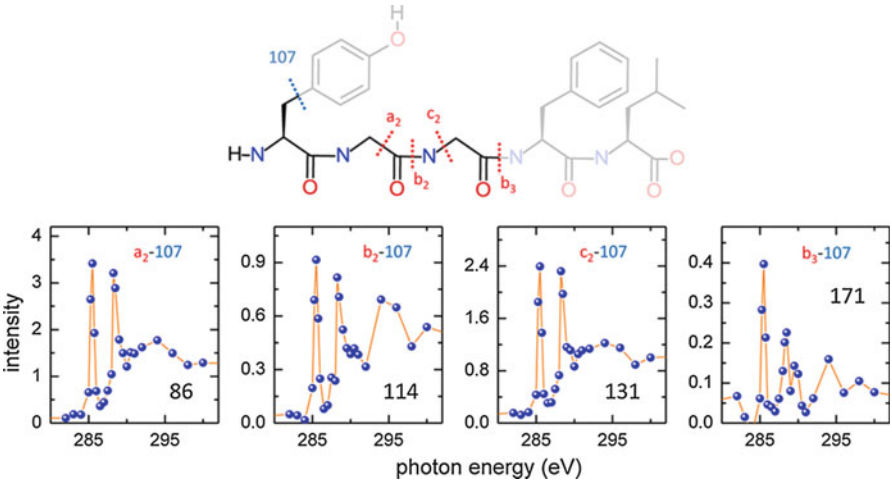

Fig. 8.19 Near-edge X-ray absorption mass spectrometry of a gas-phase protonated peptide leucine-enkephalin $[YGGFL+H]^+$ (Reprinted with permission from O. González-Magaña et al. (2009) *The journal of physical chemistry. A*, *116*, 10745 [73]. Copyright (2012) American Chemical Society)

also correlate specific transitions to specific fragmentation channels and fragmentation intensity. Interestingly, it has been found that excitations in the aromatic side chains lead to relatively little fragmentation in comparison with such excitations along the peptide backbone. It should be also pointed out that the study reported by González-Magaña and coauthors [73] clearly shows an intensive fragmentation of a relatively short peptide chain (a pentapeptide) upon soft X-ray absorption, similarly as found for its constituents – the isolated amino acids (see Sect. 5.1.1). However, this is in contrast to the larger polymer, proteins [10], and will be discussed below.

We have recently studied NEXAMS of protonated substance P peptide (Arg-Pro-Lys-Pro-Gln-Gln-Phe-Phe-Gly-Leu-Met-NH_2), as well as its nanosolvation by a controlled amount of water molecules produced by nanospray ionization using a linear ion trap coupled with the PLEIADES beamline (Giuliani et al., *to be published*). Preliminary results suggest that yield of specific fragments can be strongly dependent on the location where photon energy is injected, i.e., on C, N, or O atoms. Moreover, upon nanosolvation, the 1s excitation of oxygen atoms related to water cluster seems to become very intensive process leading to abundant water evaporation. Gas-phase NEXAFS of such systems allows distinguishing characteristic resonances.

5.5.2 Proteins

To our knowledge, the first near-K-edge X-ray spectroscopy of a protein isolated in the gas phase has been reported by Milosavljevic et al. in 2012 [10]. Using the coupling of a linear ion trap with the PLEIADES soft X-ray beamline at the SOLEIL synchrotron facility, we have performed C, N, and O near-edge ion yield

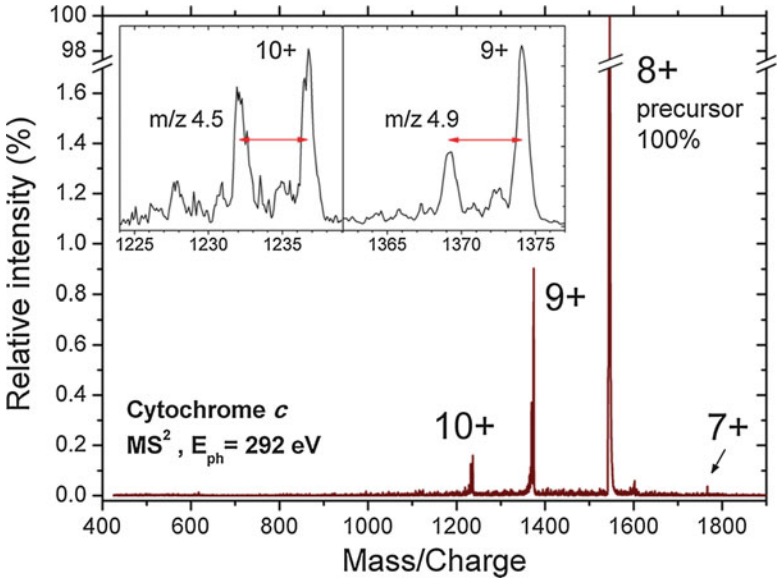

Fig. 8.20 Tandem ESI/photoionization mass spectrum of 8+ (m/z 1546) ions of cytochrome c protein from equine heart, obtained after 600 ms of irradiation at a photon energy of 292 eV (Reproduced from Milosavljević et al. [10]). The *inset* shows a zoom in the mass regions around 9+ (m/z 1374) and 10+ (m/z 1237) charge states, normalized to the same dominant peak intensity. The *arrows* mark the peaks' separations of about m/z 4.9 ± 0.1 and 4.5 ± 0.3 for the 9+ and 10+ channels, respectively, corresponding to 44 Da, tentatively assigned to CO_2 loss (Reprinted with permission from Milosavljević et al., The Journal of Physical Chemistry Letters (2012) 3, 1191 [10]. Copyright (2012) American Chemical Society)

spectroscopy of 8+ electrosprayed cations of cytochrome *c* protein (about 12 kDa). The tandem mass spectra were recorded for defined photon energies that were changed in small steps below and above the 1s core ionization thresholds.

Figure 8.20 shows a tandem ESI/photoionization mass spectrum of 8+ charge state of cytochrome *c* protein recorded at the photon energy of 292 eV. Interestingly, the protein ion appeared to be drastically less prone to fragmentation upon soft X-ray irradiation in comparison with amino acids (Sect. 5.1.1) and peptides (Sect. 5.5.1). Indeed, the main relaxation channels represent single and multiple ionization (electron ejection) accompanied with small neutral losses, which have been tentatively assigned to CO_2 losses according to the m/z difference, although it could also correspond to detachment of neutral amino acid residues. The ejected electrons from the Auger process can further trigger radiation damage [201].

Figure 8.21 shows the spectroscopy of the selected 8+ charge state precursor of the cytochrome c protein over the C, N, and O K-edges [10]. As explained above, the single precursor ionization can be exclusively a result of the resonant Auger decay upon core 1s electron resonant excitations. Indeed, the partial ion yields that correspond to the single ionization (blue circles in Fig. 8.21a–c) reveal spectral features that perfectly correspond to the NEXAFS data obtained from thin organic

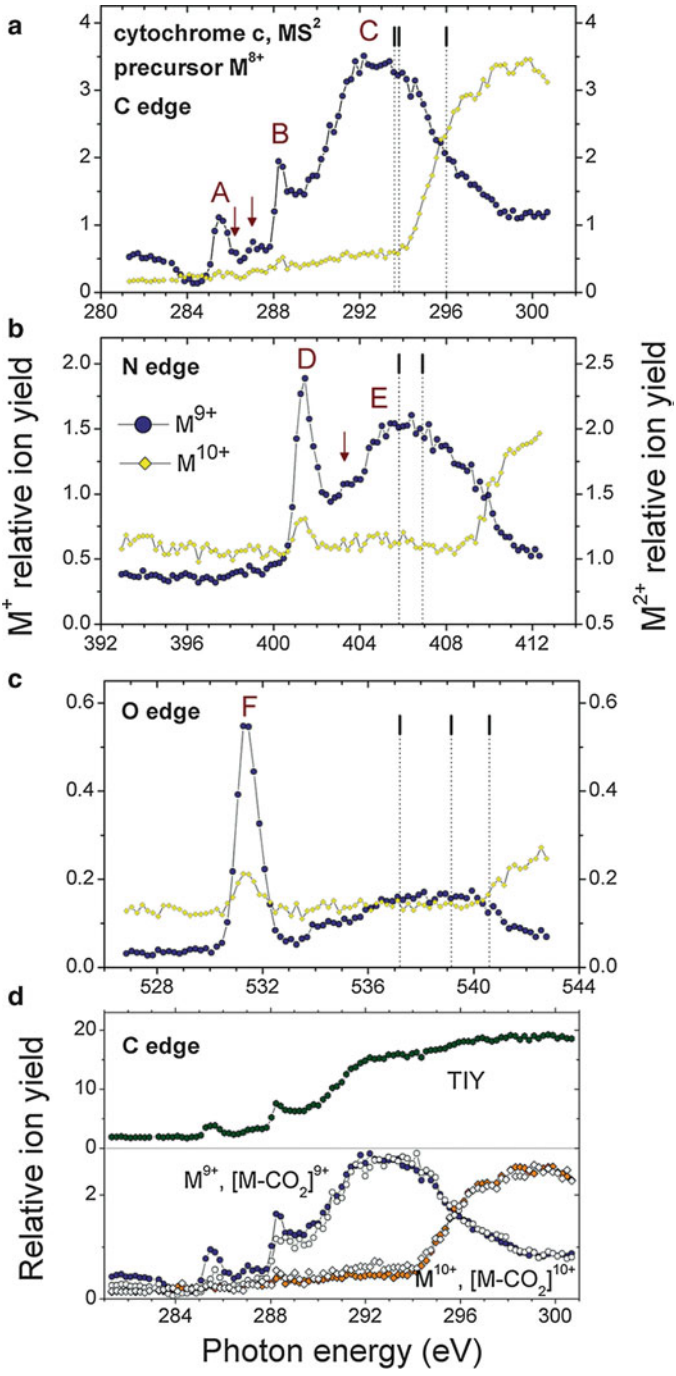

Fig. 8.21 (continued)

protein films [6, 7, 202]. In the C 1s energy domain, the peak at about 285.5 eV (denoted as A in Fig. 8.21a) can be clearly assigned to the C 1s → π* transitions associated with the aromatic rings of amino acid residues. Furthermore, the next closely lying shoulder at about 286.05 (denoted by an arrow in Fig. 8.21) has been assigned to C 1s(C − R) → $\pi^*_{C=C}$ of the Trp residue [6]. The structure at 287.0 eV can be assigned to σ^*_{C-H} resonance. The strong peak at 288.3 eV (denoted as B in Fig. 8.21a) has been assigned to the C 1s → π^*_{amide} transition. The energy position of the later structure is in perfect agreement with the previously reported values for NEXAFS spectroscopy on thin film of proteins (albumin, fibrinogen, lysozyme, ovalbumin, collagen) [6, 7]. However, interestingly, the relative intensity of this transition appeared to be much lower than expected. Indeed, the peaks corresponding to a C 1s → π^*_{amide} transition, as by a rule, dominate the NEXAFS spectra of solid protein samples, peptides, and amino acids. The lower intensity can be thus either a specificity that corresponds to the spectroscopy of large gaseous and multiply charged biopolymer ions or an experimental artifact. The authors suggested that an experimental influence could be due to carbon pollution of the different optical elements of the SR beamline [10], which induces a very low photon flux around the C 1s absorption edge (the so-called carbon deep), which was difficult to handle in the data treatment. This possibility is also supported by the fact that corresponding N and O 1s → π^*_{amide} transitions are dominant, as expected; moreover, the same was measured for the C K-edge for other trapped protein ions in further experiments, after cleaning the photon optics (see Fig. 8.22). The broad feature centered at about 293 eV (denoted as C in Fig. 8.21) is due to the overlap of various transitions, mainly associated with the σ* resonance (C−C, C−N, C−O, etc.) and dominantly related to valence and Rydberg transitions of amino acid residues merging into a broad band. Single-ionization spectra over the N 1s and O 1s K-edges are also very similar to previous NEXAFS data on proteins and polypeptides. The 1s → π^*_{amide} [1s → $\pi^*_{C=O}$(C = ONH)] transitions centered at about 401.4 eV and 531.4 eV for N and O 1s, respectively, dominate the spectra.

The experimental results by Milosavljevic et al. [10] have shown that ions of large biopolymers, such as proteins, can be investigated by means of the powerful NEXAFS spectroscopy method, isolated under well-defined conditions in the gas phase. For example, the typical resonant transitions have been well resolved by using the present method, directly pointing to the primary protein structure, in line with previous solid film NEXAFS studies. But at the same time, the present technique avoids the drawbacks related to NEXAFS spectroscopy on thin organic films and liquids, such as radiation damage occurring in condensed matter samples and an uncontrolled influence of the environmental effects in the case of studying condensed crystalline or aqueous samples.

Fig. 8.21 Single, double, and total C, N, and O K-edge photoionization yields of the 8+ charge state precursor of equine cytochrome c protein (Reprinted with permission from Milosavljević et al., The Journal of Physical Chemistry Letters (2012) 3, 1191 [10]. Copyright (2012) American Chemical Society)

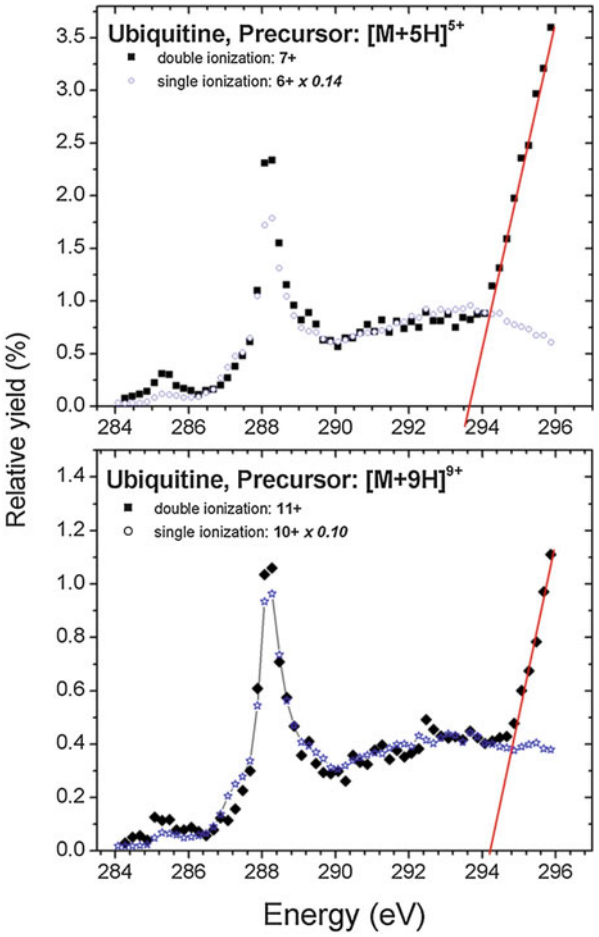

Fig. 8.22 Single (*blue circles*) and double (*black squares*) C K-edge photoionization yields of the 5+ (*top*) and 9+ (*bottom*) charge state precursor of ubiquitin protein. The single-ionization yield is normalized to the double-ionization yield

It is interesting to note that the gas-phase NEXAFS spectra of an isolated multiply protonated (8+) protein agree perfectly with NEXAFS spectroscopy on neutral thin-film protein samples. This may seem in contrast with previous microjet studies on solvated amino acids (protein building blocks), where the changing of solution pH (thus protonation/deprotonation of the biomolecule under study) has shown to affect significantly the NEXAFS resonant lines [203–205]. However, one should keep in mind that in the present case of a large gaseous protein ion, only a few protonated amino acids (according to the charge state) inside the precursor actually contribute to a possible chemical shift of the resonant transition; and resonant energy is additionally smeared out due to the contribution from different C atoms, with respect to their distance from the protonation site. Therefore, the overall effect can be negligible. Indeed, this is shown in more recent measurements for different charge states of ubiquitin protein [13]. Figure 8.22 presents single- and double-ionization yields of the 5+ and 9+ protonated precursors of ubiquitin. The experiment was performed by

coupling a commercial linear LTQ XL ion trap to the soft X-ray beamline PLEIADES at the SOLEIL synchrotron facility. For both charge state precursors (5 and 9), the ionization yields show the characteristic NEXAFS features corresponding to the C 1s → π* transitions in the aromatic amino acids at about 285.5 eV and the strong peak at 288.3 eV due to the C 1s → π^*_{amide} transitions in the peptide backbone. Clearly, these resonant excitation energies appear to be the same for both charge states, even though the level of protonation is significantly different.

The fact that the resonant core 1s transition energies to frontier molecular orbitals of a large protein are not affected by its protonation appears to be even more interesting if we consider the ternary structure of the protein. Actually, the protonation can alter its structural arrangement if the protein is free to unfold, as a consequence of minimizing the potential energy of the system [142]. Particularly, the 5+ protonated ubiquitin ion in the gas phase is still dominantly folded, while the increase of protonation to 9+ induces the unfolding of the protein [142]. Therefore, the tertiary structure of the 5+ ubiquitin precursor is drastically different from the 9+ precursor. On the other hand, there is no measurable difference in their C K-edge excitation to the molecular π* orbitals associated with aromatics and the peptide backbone. Since the core 1s electron is localized in the vicinity of the C atom, the present experiment shows that the frontier protein orbitals also appear to be rather localized and do not depend strongly on the tertiary protein structure.

Double-ionization yields of both precursors presented in Fig. 8.22 seem to exactly follow the shape of the corresponding single-ionization yields below the core ionization threshold. This confirms that double ionization below the threshold is due to the multiple resonant Auger decay – the relaxation of the core-excited species preceded by ejection of two Auger electrons. But, since the process is triggered by the same electronic transition, the spectroscopic signature is the same, as seen in Fig. 8.22. Nevertheless, above the threshold the 1s electron is directly ejected into the vacuum, and normal Auger decay becomes operative, thus reducing drastically single-ionization events on behalf of the double ionization. Therefore, the double-ionization yield allows determination of the K-edge ionization threshold of a protein under study. It is interesting to note that, in contrast to the resonant excitation, the 1s threshold energies do depend on the precursor charge state. Clearly, the ionization energy of the 9+ precursor is shifted upwards with respect to the 5+ one. However, the shift should not be the consequence of the change in the electronic structure. In the case of the protonated (positively charged) target, the departing electron also needs to overcome the Coulomb barrier, which depends both on the protonation level and the protein ternary structure [142].

5.5.3 Oligonucleotides

González-Magaña et al. [132] have investigated photon-induced fragmentation of protonated oligonucleotides in a large energy domain from 30 eV to 600 eV. The precursors under study were doubly protonated oligonucleotides $[dGCAT + 2H]^{2+}$ or $[dGTAT + 2H]^{2+}$ (the letters G, C, A, and T denoting the nucleobases guanine, cytosine, adenine, and thymine, respectively), which were isolated in a Paul trap and submitted to either soft X-ray radiation or the highly charged ions [132]. In this way,

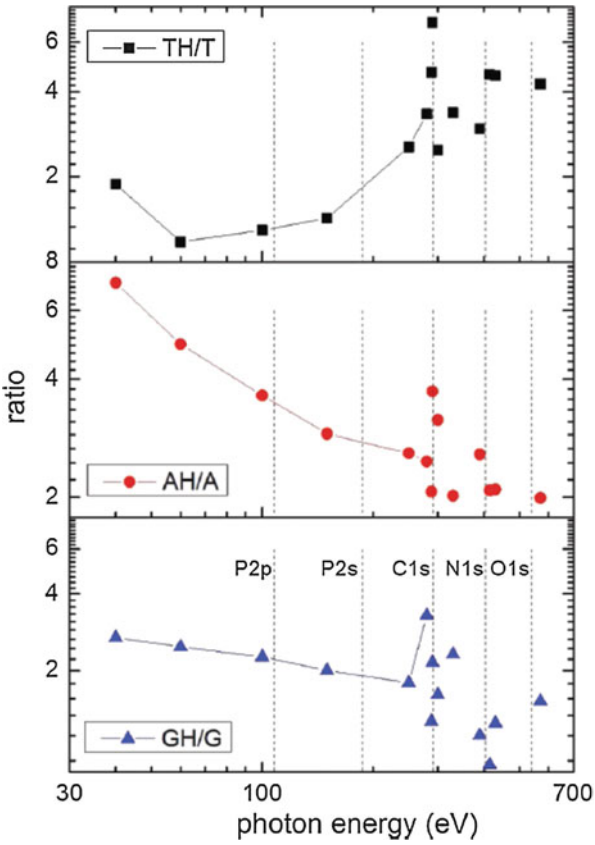

Fig. 8.23 Ratios between protonated and nonprotonated nucleobase yields for T, A, and G as a function of the photon energy (Reprinted figure with permission from Lau et al., *Physical Review A*, 87, 032702 (2013) [132]. Copyright (2013) by the American Physical Society)

the authors aimed at performing a systematic study on differences and similarities between ion- and photon-induced excitation and fragmentation mechanisms in DNA. They found qualitatively similar fragmentation patterns for both types of projectiles (ions and energetic X-ray photons). The measured fragmentation patterns revealed that nucleobases appeared to be rather stable, while deoxyribose fragments dominated the spectra.

The relative photoabsorption cross sections, as well as the photofragmentation yields for protonated and nonprotonated nucleobases spanning over a wide photon energy range, clearly show an expected increased ion production in the vicinity of C and N core 1s ionization thresholds, as a consequence of the inner-shell core formation triggering the Auger processes. However, the energy step was too coarse for fine near K-edge spectroscopic structures to be studied. Still, the authors could compare the yields of protonated and nonprotonated nucleobases as a function of the photon energy. Interestingly, they found that the ratio between protonated and nonprotonated yields depends strongly on ion velocity and photon energy. For example, a significant increase of the yield of protonated bases relative to the nonprotonated fragments is measured at resonant 1s excitation of the molecule (see Fig. 8.23).

5.5.4 Polycyclic Aromatic Hydrocarbons

Gas-phase polycyclic aromatic hydrocarbons (PAHs) have been also investigated by means of near-edge X-ray absorption mass spectrometry [111, 206, 207]. The PAHs are of great interest in many research fields such as astrochemistry/astrophysics and combustion and analytical chemistry [111]. Moreover, the investigation of the electronic properties of PAHs and the influence of certain processes such as hydrogenation to the electronic structure, under well-defined conditions, may be relevant for both the fundamental and applied nanosciences.

The experiments of Reitsma et al. [111, 207] have been performed by coupling an ion trap time-of-flight (ToF) instrument with the soft X-ray beamline U49/2-PGM1 at the BESSY II synchrotron facility. The ions were produced by an ESI, trapped in an RF Paul trap, and the product ions were analyzed using ToF. The authors have investigated the photoexcitation, photoionization, and photodissociation of gas-phase coronene cations $C_{24}H_{12}^{+}$ upon soft X-ray absorption in the C K-edge region. The relaxation of superhydrogenated gas-phase coronene cation upon resonant carbon (1s) $\rightarrow \pi^*$ transition at 285 eV was investigated by means of NEXAMS and compared to calculations [207]. The results allowed for postulating the effect of superhydrogenation on the ionization and fragmentation of PAHs. It has been found that superhydrogenation acts as a buffer that protects PAH molecules against X-ray-induced destruction. NEXAMS of coronene is further investigated by the same authors in more details [111]. NEXAMS spectra for a number of different fragmentation channels, resulting from the inner-shell excitation or ionization of the coronene precursor $C_{24}H_{12}^{+}$, were presented. The excitation of the carbon 1s electron triggers the Auger process that leads to the formation of intermediate vibrationally excited $C_{24}H_{12}^{2+}$ and $C_{24}H_{12}^{3+}$ cations that can relax by means of ejecting H atoms. Figure 8.24 presents NEXAMS spectra for different coronene dications as a function of the number of H atoms lost [111]. Figure 8.24 shows that while the formation of intact dications is mainly triggered by C 1s $\rightarrow \pi^*$ transition at about 285 eV, the formation of dications that lose 2, 4, and 6 H atoms occurs also at higher photon energies, as a consequence of different resonant processes that can be associated to σ^* and Rydberg transitions. Moreover, the dications that lost H atoms can be detected even above the core ionization threshold.

It should be noted that the gas-phase NEXAFS spectroscopy of neutral PAH molecules has been reported, as well [206]. In their experiment, Fronzoni et al. [206] used a custom-built resistively heated furnace made of stainless steel to sublimate PAH samples into the vacuum chamber. The authors could regulate the sublimation temperature and monitor the vaporization by measuring the valence photoelectron spectrum of the heated sample. The experimental setup was based on a crossed photon/molecular beam arrangement, allowing the core-level photoelectron spectroscopy. The measurements were performed at the gas-phase photoemission (GAPH) beamline at Elettra synchrotron using a VG 150 mm hemispherical electrostatic analyzer. The reported work represents a combination of experimental and theoretical study of the C1s NEXAFS and X-ray photoelectron spectroscopy allowing for a detailed investigation of the vibronic coupling in PAHs and the role of this effect in such systems.

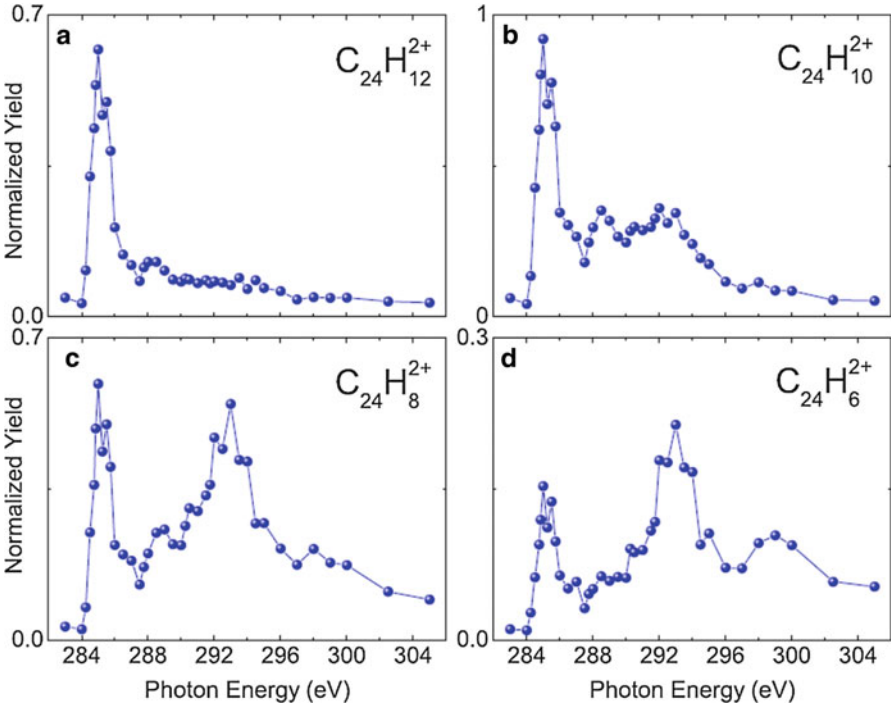

Fig. 8.24 NEXAMS spectra for $C_{24}H_{12}^{+}$ (**a**), $C_{24}H_{10}^{+}$ (**b**), $C_{24}H_{8}^{+}$ (**c**), and $C_{24}H_{6}^{+}$ (**d**), illustrating the strong dependence of the dehydrogenation on the photon energy (Reprinted with permission from Reitsma et al. (2012) *The Journal of chemical physics*, *142*, 024308 [111]. Copyright (2012), AIP Publishing LLC)

6 Conclusions and Perspectives

In recent years, the gap between NEXAFS spectroscopy studies of condensed and gas-phase matter has been shrinking. Indeed, the development of techniques allowing placement of intact species of increasing size and complexity in the gas phase has emerged, allowing study of polymers or nanoparticles. More recently, the advent of ion-trapping experiments has opened up a new area in the study of mass-selected targets.

In this chapter, we have reviewed novel experimental methods allowing performance of gas-phase NEXAFS spectroscopy of large complex species. The chapter includes a short presentation of SR sources that can provide a high-brilliance X-ray photon beam. The inner-shell studies of diluted matter are extremely photon demanding, particularly in the case of large particles that can be collected in the gas phase with extremely low partial pressures. Therefore, development of new-generation X-ray SR sources was a necessary step needed to perform such studies. The chapter further includes descriptions of general techniques used to perform inner-shell studies, with a

particular focus on X-ray action spectroscopy. Indeed, the more recent methods based on action spectroscopy offer significant improvements regarding both the sensitivity and selectivity of the technique in the case of low-density complex targets. We have also described novel techniques for sources of gas-phase targets, as well as experimental setups coupling the sources of large gas-phase targets with an X-ray beam. Finally, we review results spanning from relatively small metallic and organic molecular ions, over isolated DNA basis and amino acids representing building blocks of large biopolymers and finally including full proteins and molecular clusters.

In the present chapter, we also review the results on gas-phase NEXAFS spectroscopy of nanoparticles. Nanoparticles play an important role in our everyday lives, and in order to obtain the maximum amount of useful information on one specific system, spectroscopic and imaging techniques are often used in parallel. It has been shown that under-vacuum beams of nanoparticle have the advantages of preserving the integrity of the targets, as well as cancelling any detrimental influence of the substrate on the physical properties of the nanosystem, but also the advantage of removing any aging problem as the sample is continuously renewed. Even if the density of nanoparticles remains low in the beam, near-edge absorption spectroscopy can be performed. Moreover, it offers a mean to probe functionalized free nanoparticles where a sub-monolayer of ligands is attached to the particle. It is important to note that another way to introduce nanoparticles under vacuum is to couple the spectrometers with a liquid microjet, in which a solution containing nanoparticles forms a jet under vacuum through a capillary. The liquid jet then intercepts the synchrotron beam inside the spectrometer chamber, following which the electrons created can be analyzed [208, 209]. A recent review on the different experiments performed on nanoparticles can be found in Brown et al. [210], and this clearly highlights the capabilities of this complementary technique in tackling different questions regarding the nanoparticle/liquid interface. Moreover, wide varieties of different kinds of nanoparticles can be studied, from multilayered to functionalized or homogeneous nanoparticles. In addition, different synchrotrons are now offering liquid microjet sources or even dedicated end stations [211–213].

The variety of samples that will be accessible to X-ray spectroscopy will undoubtedly increase in the forthcoming years. Indeed, analytical chemists have developed a wide range of ionization techniques, such as atmospheric pressure MALDI, and atmospheric pressure photoionization or ASAP probe, from which the atomic and molecular community can profit. The current tendency is to increase the control on the target. The benefit of mass and charge-selected spectroscopy has allowed to gradually bridge the gap between the isolated atomic ion up to the bulk through the study of continuously controlled cluster composition. For biomolecules, the effect of the charge state on the spectroscopic properties could be evidenced for the first time. However, control on the mass and charge may not be sufficient, and conformation-specific experiments could be necessary. It is very likely that in the near future, experiments will combine mass-selected targets using ion traps in combination with ion mobility to reach conformationally selected targets. Thus, further studies will allow for reaching unprecedented control of the target to gain deeper understanding of the physicochemical and structural properties of complex systems.

References

1. Stöhr J (1992) NEXAFS spectroscopy, vol 25, Springer series in surface sciences. Springer, Berlin
2. Hähner G (2006) Near edge X-ray absorption fine structure spectroscopy as a tool to probe electronic and structural properties of thin organic films and liquids. Chem Soc Rev 35 (12):1244–1255. doi:10.1039/b509853j
3. Wu P, Yu Y, McGhee CE, Tan LH, Lu Y (2014) Applications of synchrotron-based spectroscopic techniques in studying nucleic acids and nucleic acid-functionalized nanomaterials. Adv Mater 26(46):7849–7872. doi:10.1002/adma.201304891
4. Brena B, Siegbahn PEM, Agren H (2012) Modeling near edge fine structure X-ray spectra of the manganese catalytic site for water oxidation in photosystem II. J Am Chem Soc. doi:10.1021/ja306794p
5. Zubavichus Y, Shaporenko A, Grunze M, Zharnikov M (2007) NEXAFS spectroscopy of homopolypeptides at all relevant absorption edges. J Phys Chem B 111(33):9803–9807
6. Stewart-Ornstein J, Hitchcock AP, Hernández Cruz D, Henklein P, Overhage J, Hilpert K et al (2007) Using intrinsic X-ray absorption spectral differences to identify and map peptides and proteins. J Phys Chem B 111(26):7691–7699
7. Zubavichus Y, Shaporenko A, Grunze M, Zharnikov M (2008) Is X-ray absorption spectroscopy sensitive to the amino acid composition of functional proteins? J Phys Chem B 112 (15):4478–4480. doi:10.1021/jp801248n
8. Aziz EF (2011) X-ray spectroscopies revealing the structure and dynamics of metalloprotein active centers. J Phys Chem Lett 2(4):320–326. doi:10.1021/jz1014778
9. Baio JE, Jaye C, Fischer DA, Weidner T (2014) High-throughput analysis of molecular orientation on surfaces by NEXAFS imaging of curved sample arrays. ACS Comb Sci 16 (9):449–453. doi:10.1021/co5001162
10. Milosavljević AR, Canon F, Nicolas C, Miron C, Nahon L, Giuliani A (2012) Gas-phase protein inner-shell spectroscopy by coupling an ion trap with a soft X-ray beamline. J Phys Chem Lett 3(9):1191–1196. doi:10.1021/jz300324z
11. Fenn JB, Mann M, Meng CK, Wong SF, Whitehouse CM (1990) Electrospray ionization-principles and practice. Mass Spectrom Rev 9(1):37–70. doi:10.1002/mas.1280090103
12. Aebersold R, Mann M (2003) Mass spectrometry-based proteomics. Nature 422 (6928):198–207. doi:10.1038/nature01511
13. Milosavljević AR, Nicolas C, Ranković MLJ, Canon F, Miron C, Giuliani A (2015) K-shell excitation and ionization of a gas-phase protein: interplay between electronic structure and protein folding. J Phys Chem Lett 6:3132. doi:10.1021/acs.jpclett.5b01288
14. Ivanenko DD, Pommeranchuck I (1944) On the maximal energy, obtainable in a betatron. Phys Rev 65:343
15. Schwinger J (1949) Phys Rev 75:1912
16. Schwinger J (1946) Electron radiation in high energy accelerators. Phys Rev 70:798
17. Hartman P, Tomboulian D (1952) Ultraviolet radiation from the Cornell synchrotron. Phys Rev 87(1):233
18. Codling K, Madden RP (1965) Characteristics of the "synchrotron light" from the NBS 180-MeV machine. J Appl Phys 36(2):380
19. Madden RP, Codling K (1964) Recently discovered auto-ionizing states of krypton and xenon in the λ380–600-Å region. J Opt Soc Am 54(2):268
20. Madden RP, Codling K (1963) New autoionizing atomic energy levels in He, Ne, and Ar. Phys Rev Lett 10(12):516. doi:10.1103/PhysRevLett.10.516
21. Kuntz C, Rowe EM, Gudat W, Kotani A, Toyozawa Y, Codling K et al (1979) Synchrotron radiation techniques and applications. In: Kuntz C (ed) Topics in current physics. Springer, Berlin/Heidelberg/New York
22. Motz H (1951) Applications of the radiation from fast electron beams. J Appl Phys 22(5):527

23. Motz H, Thon W, Whitehurst RN (1953) Experiments on radiation by fast electron beams. J Appl Phys 24(7):826
24. Winick H, Brown G, Halbach K, Harris J (1981) Wiggler and undulator magnets. Phys Today 34(5):50. doi:10.1063/1.2914568
25. David A (2000) Soft X-rays and extreme ultraviolet radiation: principles and applications. Cambridge University Press, Cambridge
26. Borland M (2013) Progress toward an ultimate storage ring light source. J Phys Conf Ser 425:042016
27. Johansson LC, Arnlund D, White TA, Katona G, Deponte DP, Weierstall U et al (2012) Lipidic phase membrane protein serial femtosecond crystallography. Nat Methods 9(3):263–265
28. Arnlund D, Johansson LC, Wickstrand C, Barty A, Williams GJ, Malmerberg E, Neutze R et al (2014) Visualizing a protein quake with time-resolved X-ray scattering at a free-electron laser. Nat Methods 11(9):923–926. doi:10.1038/nmeth.3067
29. Seibert MM, Ekeberg T, Maia FR, Svenda M, Andreasson J, Jönsson O et al (2011) Single mimivirus particles intercepted and imaged with an X-ray laser. Nature 470(7332):78–81
30. Chapman HN, Fromme P, Barty A, White TA, Kirian RA, Aquila A, Spence JC et al (2011) Femtosecond X-ray protein nanocrystallography. Nature 470(7332):73–77
31. Koopmann R, Cupelli K, Redecke L (2012) In vivo protein crystallization opens new routes in structural biology. Nat Methods 9(3):259
32. Loh ND, Hampton CY, Martin AV, Starodub D, Sierra RG, Barty A et al (2012) Fractal morphology, imaging and mass spectrometry of single aerosol particles in flight. Nature 486 (7404):513–517
33. Hitchcock AP, Beaulieu S, Steel T, Stöhr J, Sette F (1984) Carbon K-shell electron energy loss spectra of 1- and 2-butenes, trans-1,3-butadiene, and perfluoro-2-butene. Carbon–carbon bond lengths from continuum shape resonances. J Chem Phys 80(9):3927
34. Sette F, Stöhr J, Hitchcock AP (1984) Determination of intramolecular bond lengths in gas phase molecules from K shell shape resonances. J Chem Phys 81(11):4906
35. Stöhr J, Gland J, Kollin E, Koestner R, Johnson A, Muetterties E, Sette F (1984) Desulfurization and structural transformation of thiophene on the Pt(111) surface. Phys Rev Lett 53 (22):2161–2164
36. Guillemin R, Stolte WC, Piancastelli MN, Lindle DW (2010) Jahn-Teller coupling and fragmentation after core-shell excitation in CF_{4} investigated by partial-ion-yield spectroscopy. Phys Rev A 82(4):043427. doi:10.1103/PhysRevA.82.043427
37. Piancastelli M (1999) The neverending story of shape resonances. J Electron Spectrosc Relat Phenom 100(1–3):167–190. doi:10.1016/S0368-2048(99)00046-8
38. Guillemin R, Stolte WC, Lindle DW (2009) Fragmentation of formic acid following photoexcitation around the carbon K edge. J Phys B Atomic Mol Phys 42(12):125101. doi:10.1088/0953-4075/42/12/125101
39. Kock E-E (ed) (1983) Handbook on synchrotron radiation. North Holland Pub Co, Amsterdam
40. Quack M, Merkt F (eds) (2011) Handbook of high-resolution spectroscopy. John Wiley, New York, p 2182
41. Bagus PS, Ilton ES, Nelin CJ (2013) The interpretation of XPS spectra: insights into materials properties. Surf Sci Rep 68(2):273–304
42. Ueda K (2003) High-resolution inner-shell spectroscopies of free atoms and molecules using soft-x-ray beamlines at the third-generation synchrotron radiation sources. J Phys B Atomic Mol Phys 36(4):R1–R47. doi:10.1088/0953-4075/36/4/201
43. Miron C, Morin P (2011) High-resolution inner-shell photo-ionization photoelectron and coincidence spectroscopy. In: Quack M, Merkt F (eds) Handbook of high-resolution spectroscopy, vol 3. John Wiley, New York, pp 1655–1689
44. Björneholm O, Öhrwall G, Tchaplyguine M (2009) Free clusters studied by core-level spectroscopies. Nucl Instrum Methods Phys Res, Sect A 601(1–2):161–181. doi:10.1016/j.nima.2008.12.222

45. Makarova AA, Grachova EV, Krupenya DV, Vilkov O, Fedorov A, Usachov D et al (2014) Insight into the electronic structure of the supramolecular "rods-in-belt" AuICuI and AuIAgI self-assembled complexes from X-ray photoelectron and absorption spectroscopy. J Electron Spectrosc Relat Phenom 192:26–34
46. Miron C, Patanen M (2014) Synchrotron-radiation-based soft X-ray electron spectroscopy applied to structural and chemical characterization of isolated species, from molecules to nanoparticles. Adv Mater 26:7911–7916. doi:10.1002/adma.201304837
47. Schramm T, Ganteför G, Bodi A, Hemberger P, Gerber T, von Issendorff B (2014) Photoelectron spectroscopy of size-selected cluster ions using synchrotron radiation. Appl Phys A 115 (3):771–779. doi:10.1007/s00339-014-8434-z
48. Tchaplyguine M, Peredkov S, Rosso A, Schulz J, Öhrwall G, Lundwall M et al (2007) Direct observation of the non-supported metal nanoparticle electron density of states by X-ray photoelectron spectroscopy. Eur Phys J D 45(2):295–299
49. Tchaplyguine M, Zhang C, Andersson T, Björneholm O (2014) Tuning the oxidation degree in sub-10nm silver-oxide nanoparticles: from Ag2O monoxide to AgOx(x > 1) superoxide. Chem Phys Lett 600:96–102
50. Bahn J, Oelßner P, Köther M, Braun C, Senz V, Palutke S et al (2012) Pb 4f photoelectron spectroscopy on mass-selected anionic lead clusters at FLASH. New J Phys 14(7):075008
51. Sublemontier O, Nicolas C, Aureau D, Patanen M, Kintz H, Liu X et al (2014) X-ray photoelectron spectroscopy of isolated nanoparticles. J Phys Chem Lett 5(19): 3399–3403
52. Antonsson E, Bresch H, Lewinski R (2013) Free nanoparticles studied by soft X-rays. Chem Phys Lett 559:1–11
53. Baer DR, Engelhard MH (2010) XPS analysis of nanostructured materials and biological surfaces. J Electron Spectrosc Relat Phenom 178–179:415–432
54. Meinen J, Khasminskaya S, Eritt M, Leisner T, Antonsson E, Langer B, Rühl E (2010) Core level photoionization on free sub-10-nm nanoparticles using synchrotron radiation. Rev Sci Instrum 81(8):085107
55. Mysak ER, Starr DE, Wilson KR, Bluhm H (2010) Note: A combined aerodynamic lens/ ambient pressure x-ray photoelectron spectroscopy experiment for the on-stream investigation of aerosol surfaces. Rev Sci Instrum 81(1):016106
56. Wilson KR, Bluhm H, Ahmed M (2011) Fundamentals and applications in aerosol spectroscopy, "Aerosol photoemission", fundamentals and applications in aerosol spectroscopy. In: Signorell R, Reid JR (eds). Taylor & Francis Inc, Philadelphia, p 367
57. Shigemasa E, Adachi J, Oura M, Yagishita A (1995) Angular distributions of 1sσ{} photoelectrons from fixed-in-space {{\mathrm N}}_{2} molecules. Phys Rev Lett 74(3):359–362. doi:10.1103/PhysRevLett.74.359
58. Dörner R, Bräuning H, Feagin JM, Mergel V, Jagutzki O, Spielberger L et al (1998) Photo-double-ionization of He: fully differential and absolute electronic and ionic momentum distributions. Phys Rev A 57(2):1074–1090. doi:10.1103/PhysRevA.57.1074
59. Ueda K, Simon M, Miron C, Leclercq N, Guillemin R, Morin P, Tanaka S (1999) Correlation between nuclear motion in the core-excited CF4 molecule and molecular dissociation after resonant auger decay. Phys Rev Lett 83(19):3800–3803
60. Prümper G, Carravetta V, Muramatsu Y, Tamenori Y, Kitajima M, Tanaka H et al (2007) Electron transfer during the dissociation of CH_{3}F^{+} produced by resonant photoemission following F 1s excitation. Phys Rev A 76(5):52705. doi:10.1103/PhysRevA.76.052705
61. Liu XJ, Prümper G, Kukk E, Sankari R, Hoshino M, Makochekanwa C et al (2005) Site-selective ion production of the core-excited CH_{3}F molecule probed by Auger-electron–ion coincidence measurements. Phys Rev A 72(4):42704. doi:10.1103/PhysRevA.72.042704
62. Miron C, Morin P (2009) High-resolution inner-shell coincidence spectroscopy. Nucl Instrum Methods Phys Res Sect A, 601(1–2, Sp. Iss. SI):66–77. doi:10.1016/j.nima.2008.12.104
63. Dörner R, Mergel V, Jagutzki O, Spielberger L, Ullrich J, Moshammer R, Schmidt-Böcking H (2000) Cold target recoil ion momentum spectroscopy: a 'momentum microscope' to

view atomic collision dynamics. Phys Rep 330(2–3):95–192. doi:10.1016/S0370-1573(99)00109-X
64. Ullrich J, Moshammer R, Dorn A, Dörner R, Schmidt LPH, Schmidt-Böcking H (2003) Recoil-ion and electron momentum spectroscopy: reaction-microscopes. Rep Prog Phys 66:1463. doi:10.1088/0034-4885/66/9/203
65. Ceolin D, Miron C, Simon M, Morin P (2004) Auger electron-ion coincidence studies to probe molecular dynamics. J Electron Spectrosc Relat Phenom, 141(2–3, Sp. Iss. SI):171–181. doi:10.1016/j.elspec.2004.06.014
66. Rühl E, Schmale C, Schmelz HC, Baumgärtel H (1992) The double ionization potentials of argon clusters. Chem Phys Lett 191(5):430–434
67. Mucke M, Braune M, Barth S, Förstel M, Lischke T, Ulrich V et al (2010) A hitherto unrecognized source of low-energy electrons in water. Nat Phys 6(2):143–146
68. Biester H, Besnard M, Dujardin G, Hellner L, Koch E (1987) Photoemission of pairs of electrons from rare-gas solids. Phys Rev Lett 59(12):1277–1280
69. Herrmann R, Samarin S, Schwabe H, Kirschner J (1998) Two electron photoemission in solids. Phys Rev Lett 81(10):2148–2151. doi:10.1103/PhysRevLett.81.2148
70. Huth M, Chiang C-T, Trützschler A, Schumann FO, Kirschner J, Widdra W (2014) Electron pair emission detected by time-of-flight spectrometers: recent progress. Appl Phys Lett 104(6):061602
71. Schumann FO, Behnke L, Li CH, Kirschner J (2013) Exploring highly correlated materials via electron pair emission: the case of NiO/Ag(100). J Phys Condens Matter 25(9):094002. doi:10.1088/0953-8984/25/9/094002
72. Giuliani A, Milosavljević AR, Canon F, Nahon L (2014) Contribution of synchrotron radiation to photoactivation studies of biomolecular ions in the gas phase. Mass Spectrom Rev 33(6):424–441. doi:10.1002/mas.21398
73. González-Magaña O, Reitsma G, Tiemens M, Boschman L, Hoekstra R, Schlathölter T (2012) Near-edge X-ray absorption mass spectrometry of a gas-phase peptide. J Phys Chem A 116(44):10745–10751. doi:10.1021/jp307527b
74. Baer T, Dunbar RC (2010) Ion spectroscopy: where did it come from; where is it now; and where is it going? J Am Soc Mass Spectrom 21(5):681–693. doi:10.1016/j.jasms.2010.01.028
75. Lucas CB (2013) Atomic and molecular beams: production and collimation. CRC Press, 6000 Broken Sound Pkwy NW - Boca Raton FL, p 392
76. Touboul D, Gaie-Levrel F, Garcia GA, Nahon L, Poisson L, Schwell M, Hochlaf M (2013) VUV photoionization of gas phase adenine and cytosine: a comparison between oven and aerosol vaporization. J Chem Phys 138(9):094203. doi:10.1063/1.4793734
77. Bernstein ER (1990) Atomic and molecular clusters. In: Bernstein ER (ed). Elsevier, Amsterdam/Oxford/New York/Tokyo, p 805
78. Wegner K, Piseri P, Tafreshi HV, Milani P (2006) Cluster beam deposition: a tool for nanoscale science and technology. J Phys D Appl Phys 39(22):R439–R459
79. Lindblad A, Söderström J, Nicolas C, Robert E, Daniel G, Miron C (2013) A multi purpose source chamber at the PLEIADES beamline at SOLEIL for spectroscopic studies of isolated species: cold molecules, clusters, and nanoparticles. Rev Sci Instrum 84:113105. doi:10.1063/1.4829718
80. Wilson KR, Jimenez-Cruz M, Nicolas C, Belau L, Leone SR, Ahmed M (2006) Thermal vaporization of biological nanoparticles: fragment-free vacuum ultraviolet photoionization mass spectra of tryptophan, phenylalanine-glycine- glycine, and β-carotene. J Phys Chem A 110(6):2106–2113
81. Wilson KR, Belau L, Nicolas C, Jimenez-Cruz M, Leone SR, Ahmed M (2006) Direct determination of the ionization energy of histidine with VUV synchrotron radiation. Int J Mass Spectrom 249–250:155–161
82. Gaie-Levrel F, Garcia GA, Schwell M, Nahon L (2011) VUV state-selected photoionization of thermally-desorbed biomolecules by coupling an aerosol source to an imaging photoelectron/photoion coincidence spectrometer: case of the amino acids tryptophan and phenylalanine. Phys Chem Chem Phys 13(15):7024–7036

83. Tia M, Cunha de Miranda B, Daly S, Gaie-Levrel F, Garcia GA, Nahon L, Powis I (2014) VUV photodynamics and chiral asymmetry in the photoionization of gas phase alanine enantiomers. J Phys Chem A 118(15):2765–2779
84. Isaacman G, Wilson KR, Chan AWH, Worton DR, Kimmel JR, Nah T et al (2012) Improved resolution of hydrocarbon structures and constitutional isomers in complex mixtures using gas chromatography-vacuum ultraviolet-mass spectrometry. Anal Chem 84(5):2335–2342
85. Liu P, Ziemann PJ, Kittelson DB, McMurry PH (1995) Generating particle beams of controlled dimensions and divergence. 1. Theory of particle motion in aerodynamic lenses and nozzle expansions. Aerosol Sci Technol 22(3):293–313. doi:10.1080/02786829408959748
86. Liu P, Ziemann PJ, Kittelson DB, McMurry PH (1995) Generating particle beams of controlled dimensions and divergence. 2. Experimental evaluation of particle motion in aerodynamic lenses and nozzle expansions. Aerosol Sci Technol 22(3):314–324. doi:10.1080/02786829408959749
87. Zhang XF, Smith KA, Worsnop DR, Jimenez JL, Jayne JT, Kolb CE et al (2004) Numerical characterization of particle beam collimation: part II – integrated aerodynamic-lens-nozzle system. Aerosol Sci Technol 38(6):619–638. doi:10.1080/02786820490479833
88. Zhang XF, Smith KA, Worsnop DR, Jimenez J, Jayne JT, Kolb CE (2002) A numerical characterization of particle beam collimation by an aerodynamic lens-nozzle system: part I. An individual lens or nozzle. Aerosol Sci Technol 36(5):617–631. doi:10.1080/02786820252883856
89. Jayne JT, Leard DC, Zhang XF, Davidovits P, Smith KA, Kolb CE, Worsnop DR (2000) Development of an aerosol mass spectrometer for size and composition analysis of submicron particles. Aerosol Sci Technol 33(1–2):49–70. doi:10.1080/027868200410840
90. Headrick JM, Schrader PE, Michelsen HA (2013) Radial-profile and divergence measurements of combustion-generated soot focused by an aerodynamic-lens system. J Aerosol Sci 58:158–170. doi:10.1016/j.jaerosci.2013.01.002
91. Wang X, Kruis FE, McMurry PH (2005) Aerodynamic focusing of nanoparticles: I. Guidelines for designing aerodynamic lenses for nanoparticles. Aerosol Sci Tech 39(7):611–623
92. Tafreshi HV, Benedek G, Piseri P, Vinati S, Barborini E, Milani P (2002) A simple nozzle configuration for the production of low divergence supersonic cluster beam by aerodynamic focusing. Aerosol Sci Tech 36(5):593–606
93. Lee D, Lee KS (2010) Aerodynamic lens. Google Patents, US 7652247 B2
94. Wang X, Gidwani A, Girshick S, McMurry P (2005) Aerodynamic focusing of nanoparticles: II. Numerical simulation of particle motion through aerodynamic lenses. Aerosol Sci Technol 39(7):624–636
95. Tafreshi H, Piseri P, Barborini E, Benedek G, Milani P (2002) Simulation on the effect of Brownian motion on nanoparticle trajectories in a pulsed microplasma cluster source. J Nanoparticle Res 4(6):511–524
96. Lewinski R, Graf C, Langer B, Flesch R, Bresch H, Wassermann B, Rühl E (2009) Size-effects in clusters and free nanoparticles probed by soft X-rays. Eur Phys J Spec Top 169(1): 67–72
97. Shrivastava M, Gidwani A, Jung HS (2009) Modeling oxidation of soot particles within a laminar aerosol flow reactor using computational fluid dynamics. Aerosol Sci Tech 43 (12):1218–1229
98. Wang X, McMurry PH, Kruis E (2009) Aerodynamic focusing of nanoparticle or cluster beams. Google Patents, US 7476851 B2
99. Piseri P, Tafreshi HV, Milani P (2004) Manipulation of nanoparticles in supersonic beams for the production of nanostructured materials. Curr Opin Solid State Mater Sci 8(3–4):195–202
100. Piseri P, Podestà A, Barborini E, Milani P (2001) Production and characterization of highly intense and collimated cluster beams by inertial focusing in supersonic expansions. Rev Sci Instrum 72(5):2261
101. Martinez F, Bandelow S, Breitenfeldt C, Marx G, Schweikhard L, Vass A, Wienholtz F (2014) Upgrades at ClusterTrap and latest results. Int J Mass Spectrom 365–366:266–274

102. Sturm S, Wagner A, Schabinger B, Blaum K (2011) Phase-sensitive cyclotron frequency measurements at ultralow energies. Phys Rev Lett 107(14):143003
103. Grimm M, Langer B, Schlemmer S, Lischke T, Becker U, Widdra W et al (2006) Charging mechanisms of trapped element-selectively excited nanoparticles exposed to soft X rays. Phys Rev Lett 96(6):066801
104. Gerlich D (2003) Molecular ions and nanoparticles in RF and AC traps. Hyperfine Interact 146/147(1–4):293–306
105. Shu J, Wilson KR, Ahmed M, Leone SR (2006) Coupling a versatile aerosol apparatus to a synchrotron: vacuum ultraviolet light scattering, photoelectron imaging, and fragment free mass spectrometry. Rev Sci Instrum 77(4):043106
106. Thissen R, Bizau J, Blancard C, Coreno M, Dehon C, Franceschi P et al (2008) Photoionization cross section of Xe+ ion in the pure 5p5 P3/22 ground level. Phys Rev Lett 100 (22):223001. doi:10.1103/PhysRevLett.100.223001
107. Marrs R, Elliott S, Knapp D (1994) Production and trapping of hydrogenlike and bare uranium ions in an electron beam ion trap. Phys Rev Lett 72(26):4082–4085. doi:10.1103/PhysRevLett.72.4082
108. Epp S, López-Urrutia J, Brenner G, Mäckel V, Mokler P, Treusch R et al (2007) Soft X-Ray laser spectroscopy on trapped highly charged ions at FLASH. Phys Rev Lett 98(18):183001. doi:10.1103/PhysRevLett.98.183001
109. Hirsch K, Lau JT, Klar P, Langenberg A, Probst J, Rittmann J et al (2009) X-ray spectroscopy on size-selected clusters in an ion trap: from the molecular limit to bulk properties. J Phys B Atomic Mol Phys 42(15):154029. doi:10.1088/0953-4075/42/15/154029
110. Heiz U, Vanolli F, Trento L, Schneider W-D (1997) Chemical reactivity of size-selected supported clusters: an experimental setup. Rev Sci Instrum 68(5):1986. doi:10.1063/1.1148113
111. Reitsma G, Boschman L, Deuzeman MJ, Hoekstra S, Hoekstra R, Schlathölter T (2015) Near edge X-ray absorption mass spectrometry on coronene. J Chem Phys 142(2):024308. doi:10.1063/1.4905471
112. Ryding MJ, Giuliani A, Patanen M, Niskanen J, Simões G, Miller GBS et al (2014) X-ray induced fragmentation of size-selected salt cluster-ions stored in an ion trap. RSC Adv 4 (88):47743–47751. doi:10.1039/C4RA09787D
113. Cole RB (2010) Electrospray and MALDI mass spectrometry: fundamentals, instrumentation, practicalities, and biological applications, 2nd edn. Wiley, Hoboken, p 896
114. Cox JT, Marginean I, Smith RD, Tang K (2015) On the ionization and ion transmission efficiencies of different ESI-MS interfaces. J Am Soc Mass Spectrom 26(1):55–62. doi:10.1007/s13361-014-0998-5
115. Robb D, Covey T, Bruins A (2000) Atmospheric pressure photoionization: an ionization method for liquid chromatography-mass spectrometry. Anal Chem 72(15):3653–3659
116. Song L, Wellman AD, Yao H, Adcock J (2007) Electron capture atmospheric pressure photoionization mass spectrometry: analysis of fullerenes, perfluorinated compounds, and pentafluorobenzyl derivatives. Rapid Commun Mass Spectrom 21(8):1343–1351. doi:10.1002/rcm.2963
117. Peart B, Stevenson JG, Dolder KT (1973) Measurements of cross sections for the ionization of Ba+ by energy resolved electrons. J Phys B Atomic Mol Phys 6(1):146–149. doi:10.1088/0022-3700/6/1/016
118. Lyon IC, Peart B, West JB, Dolder K (1986) Measurements of absolute cross sections for the photoionisation of Ba+ ions. J Phys B Atomic Mol Phys 19(24):4137–4147. doi:10.1088/0022-3700/19/24/015
119. Kjeldsen H, Folkmann F, Elp JV, Knudsen H, West JB, Andersen T (2005) Absolute measurements of photoionization cross-sections for ions. Nucl Instrum Methods Phys Res Sect B 234(3):349–361. doi:10.1016/j.nimb.2005.01.011
120. Kjeldsen H (2006) Photoionization cross sections of atomic ions from merged-beam experiments. J Phys B Atomic Mol Phys 39(21):R325–R377. doi:10.1088/0953-4075/39/21/R01

121. Bizau JM, Cubaynes D, Al Shorman MM, Guilbaud S, Blancard C, Lemaire J et al (2012) Photoionization of atomic and molecular positively charged ions. J Phys Conf Ser 399:012002. doi:10.1088/1742-6596/399/1/012002
122. Gharaibeh MF, Bizau JM, Cubaynes D, Guilbaud S, El Hassan N, Al Shorman MM et al (2011) K-shell photoionization of singly ionized atomic nitrogen: experiment and theory. J Phys B Atomic Mol Phys 44:175208. doi:10.1088/0953-4075/44/17/175208
123. Bizau JM, Blancard C, Coreno M, Cubaynes D, Dehon C, El Hassan N et al (2011) Photoionization study of Kr+ and Xe+ ions with the combined use of a merged-beam set-up and an ion trap. J Phys B Atomic Mol Phys 44(5):055205. doi:10.1088/0953-4075/44/5/055205
124. Bizau JM, Cubaynes D, Richter M, Wuilleumier F, Obert J, Putaux JC (1992) The combined use of a singly charged ion-beam and undulator radiation for photoelectron spectrometry studies on atomic ions. Rev Sci Instrum 63:1389–1392, Univ Paris 11, Inst Phys Nucl, F-91405 Orsay, France
125. Bizau JM, Cubaynes D, Richter M, Wuilleumier FJ, Obert J, Putaux JC et al (1991) First observation of photoelectron spectra emitted in the photoionization of a singly charged-ion beam with synchrotron radiation. Phys Rev Lett 67(5):576–579
126. Senz V, Fischer T, Oelßner P, Tiggesbäumker J, Stanzel J, Bostedt C et al (2009) Core-Hole Screening as a Probe for a Metal-to-Nonmetal Transition in Lead Clusters. Phys Rev Lett 102 (13):138303. doi:10.1103/PhysRevLett.102.138303
127. Dunbar RC (2014) In the beginning was H2+: mass spectrometry and the molecular spectroscopy of gas-phase ions. Int J Mass Spectrom. doi:10.1016/j.ijms.2014.07.049
128. Dunbar RC (2000) Photodissociation of trapped ions. Int J Mass Spectrom 200:571–589
129. Antoine R, Dugourd P (2011) Visible and ultraviolet spectroscopy of gas phase protein ions. Phys Chem Chem Phys 13(37):16494–16509. doi:10.1039/c1cp21531k
130. Peredkov S, Neeb M, Eberhardt W, Meyer J, Tombers M, Kampschulte H, Niedner-Schatteburg G (2011) Spin and orbital magnetic moments of free nanoparticles. Phys Rev Lett 107(23):233401. doi:10.1103/PhysRevLett.107.233401
131. Peredkov S, Savci A, Peters S, Neeb M, Eberhardt W, Kampschulte H et al (2011) X-ray absorption spectroscopy of mass-selected transition metal clusters using a cyclotron ion trap: an experimental setup for measuring XMCD spectra of free clusters. J Electron Spectrosc Relat Phenom 184(3–6):113–118. doi:10.1016/j.elspec.2010.12.031
132. González-Magaña O, Tiemens M, Reitsma G, Boschman L, Door M, Bari S et al (2013) Fragmentation of protonated oligonucleotides by energetic photons and Cq+ ions. Phys Rev A 87(3):032702. doi:10.1103/PhysRevA.87.032702
133. Lau JT, Rittmann J, Zamudio-Bayer V, Vogel M, Hirsch K, Klar P et al (2008) Size dependence of L2,3 branching ratio and 2p core-hole screening in X-ray absorption of metal clusters. Phys Rev Lett 101(15):153401. doi:10.1103/PhysRevLett.101.153401
134. Kravis SD, Church D, Johnson B, Meron M, Jones K, Levin J et al (1991) Inner-shell photoionization of stored positive ions using synchrotron radiation. Phys Rev Lett 66 (23):2956–2959. doi:10.1103/PhysRevLett.66.2956
135. Bari S, Gonzalez-Magaña O, Reitsma G, Werner J, Schippers S, Hoekstra R, Schlathölter T (2011) Photodissociation of protonated leucine-enkephalin in the VUV range of 8–40 eV. J Chem Phys 134(2):024314. doi:10.1063/1.3515301
136. González-Magaña O, Reitsma G, Bari S, Hoekstra R, Schlathölter T (2012) Length effects in VUV photofragmentation of protonated peptides. Phys Chem Chem Phys 14(13):4351–4354. doi:10.1039/c2cp23470j
137. Milosavljević AR, Nicolas C, Gil J, Canon F, Réfrégiers M, Nahon L, Giuliani A (2012) VUV synchrotron radiation: a new activation technique for tandem mass spectrometry. J Synchrotron Radiat 19(Pt 2):174–178. doi:10.1107/S0909049512001057
138. Schwartz JC, Senko MW (2002) A two-dimensional quadrupole ion trap mass spectrometer. J Am Soc Mass Spectrom 13(6):659–669. doi:10.1016/S1044-0305(02)00384-7

139. Thelen JJ, Miernyk JA (2012) The proteomic future: where mass spectrometry should be taking us. Biochem J 444(2):169–181
140. Canon F, Milosavljević AR, van der Rest G, Réfrégiers M, Nahon L, Sarni-Manchado P et al (2013) Photodissociation and dissociative photoionization mass spectrometry of proteins and noncovalent protein-ligand complexes. Angew Chem Int Ed Engl 52(32):8377–8381. doi:10.1002/anie.201304046
141. Canon F, Milosavljevic AR, Nahon L, Giuliani A (2015) Action spectroscopy of a protonated peptide in the ultraviolet range. Phys Chem Chem Phys. doi:10.1039/C4CP04762A
142. Giuliani A, Milosavljević AR, Hinsen K, Canon F, Nicolas C, Réfrégiers M, Nahon L (2012) Structure and charge-state dependence of the gas-phase ionization energy of proteins. Angew Chem Int Ed Engl 51(38):9552–9556. doi:10.1002/anie.201204435
143. Milosavljević AR, Nicolas C, Lemaire J, Dehon C, Thissen R, Bizau J-M et al (2011) Photoionization of a protein isolated in vacuo. Phys Chem Chem Phys 13 (34):15432–15436. doi:10.1039/c1cp21211g
144. Milosavljević AR, Giuliani A, Nicolas C, Gil J-F, Lemaire J, Réfrégiers M, Nahon L (2010) Gas-phase spectroscopy of a protein. J Phys Conf Ser 257(1992):012006. doi:10.1088/1742-6596/257/1/012006
145. Milosavljević AR, Cerovski VZ, Canon F, Nahon L, Giuliani A (2013) Nanosolvation-induced stabilization of a protonated peptide dimer isolated in the gas phase. Angew Chem Int Ed Engl 52(28):7286–7290. doi:10.1002/anie.201301667
146. Milosavljević AR, Cerovski VZ, Canon F, Ranković ML, Škoro N, Nahon L, Giuliani A (2014) Energy-dependent UV photodissociation of gas-phase adenosine monophosphate nucleotide ions: the role of a single solvent molecule. J Phys Chem Lett 5:1994–1999. doi:10.1021/jz500696b
147. Bolognesi P, Mattioli G, O'Keeffe P, Feyer V, Plekan O, Ovcharenko Y et al (2009) Investigation of halogenated pyrimidines by X-ray photoemission spectroscopy and theoretical DFT methods. J Phys Chem A 113(48):13593–13600. doi:10.1021/jp908512v
148. Bolognesi P, O'Keeffe P, Ovcharenko Y, Coreno M, Avaldi L, Feyer V et al (2010) Pyrimidine and halogenated pyrimidines near edge x-ray absorption fine structure spectra at C and N K-edges: experiment and theory. J Chem Phys 133(3):034302. doi:10.1063/1.3442489
149. Bolognesi P, O'Keeffe P, Feyer V, Plekan O, Prince K, Coreno M et al (2010) Inner shell excitation, ionization and fragmentation of pyrimidine. J Phys Conf Ser 212:012002. doi:10.1088/1742-6596/212/1/012002
150. Feyer V, Plekan O, Richter R, Coreno M, Vall-llosera G, Prince KC et al (2009) Tautomerism in cytosine and uracil: an experimental and theoretical core level spectroscopic study. J Phys Chem A 113(19):5736–5742. doi:10.1021/jp900998a
151. Plekan O, Feyer V, Richter R, Coreno M, Vall-Llosera G, Prince KC et al (2009) An experimental and theoretical core-level study of tautomerism in guanine. J Phys Chem A 113(33):9376–9385. doi:10.1021/jp903209t
152. Feyer V, Plekan O, Richter R, Coreno M, de Simone M, Prince KC et al (2010) Tautomerism in cytosine and uracil: a theoretical and experimental X-ray absorption and resonant auger study. J Phys Chem A 114(37):10270–10276. doi:10.1021/jp105062c
153. Giuliano BM, Feyer V, Prince KC, Coreno M, Evangelisti L, Melandri S, Caminati W (2010) Tautomerism in 4-hydroxypyrimidine, S-methyl-2-thiouracil, and 2-thiouracil. J Phys Chem A 114:12725–12730
154. Feyer V, Plekan O, Kivim A, Prince KC, Moskovskaya TE, Zaytseva IL et al (2011) Comprehensive core-level study of the effects of isomerism halogenation, and methylation on the tautomeric equilibrium of cytosine. J Phys Chem A 115(26):7722–7733
155. Hua W, Gao B, Li S, Ågren H, Luo Y (2010) Refinement of DNA structures through near-edge X-ray absorption fine structure analysis: applications on guanine and cytosine nucleobases, nucleosides, and nucleotides. J Phys Chem B 114:13214–13222. doi:10.1021/jp1034745

156. Itälä E, Ha DT, Kooser K, Huels MA, Rachlew E, Nõmmiste E et al (2011) Molecular fragmentation of pyrimidine derivatives following site-selective carbon core ionization. J Electron Spectrosc Relat Phenom 184(3–6):119–124. doi:10.1016/j.elspec.2011.01.007
157. Itälä E, Ha DT, Kooser K, Rachlew E, Huels MA, Kukk E (2010) Fragmentation patterns of core-ionized thymine and 5-bromouracil. J Chem Phys 133(15):154316. doi:10.1063/1.3505140
158. Itälä E, Ha DT, Kooser K, Nõmmiste E, Joost U, Kukk E (2011) Fragmentation patterns of core ionized uracil. Int J Mass Spectrom 306(1):82–90. doi:10.1016/j.ijms.2011.07.006
159. Itälä E, Huels MA, Rachlew E, Kooser K, Hägerth T, Kukk E (2013) A comparative study of dissociation of thymidine molecules following valence or core photoionization. J Phys B Atomic Mol Phys 46(21):215102. doi:10.1088/0953-4075/46/21/215102
160. Ha DT, Huels MA, Huttula M, Urpelainen S, Kukk E (2011) Experimental and ab initio study of the photofragmentation of DNA and RNA sugars. Phys Rev A 84(3):033419. doi:10.1103/PhysRevA.84.033419
161. Itälä E, Kooser K, Rachlew E, Huels MA, Kukk E (2014) Soft x-ray ionization induced fragmentation of glycine. J Chem Phys 140(23):234305. doi:10.1063/1.4882648
162. Laksman J, Kooser K, Levola H, Ita E, Ha DT, Rachlew E, Kukk E (2014) Dissociation pathways in the cysteine dication after site-selective core ionization. J Phys Chem B 118 (40):11688–11695
163. Ha DT, Wang Y, Alcamí M, Itälä E, Kooser K, Urpelainen S et al (2014) Fragmentation dynamics of doubly charged methionine in the gas phase. J Phys Chem A 118(8):1374–1383. doi:10.1021/jp4113238
164. Feyer V, Plekan O, Richter R, Coreno M, Prince KC, Carravetta V (2009) Photoemission and photoabsorption spectroscopy of glycyl-glycine in the gas phase. J Phys Chem A 113 (40):10726–10733. doi:10.1021/jp906843j
165. Feyer V, Plekan O, Richter R, Coreno M, Prince KC, Carravetta V (2008) Core level study of alanine and threonine. J Phys Chem A 112(34):7806–7815. doi:10.1021/jp803017y
166. Zhang W, Carravetta V, Plekan O, Feyer V, Richter R, Coreno M, Prince KC (2009) Electronic structure of aromatic amino acids studied by soft x-ray spectroscopy. J Chem Phys 131 (2009):035103. doi:10.1063/1.3168393
167. Li H, Hua W, Lin Z, Luo Y (2012) First-principles study on core-level spectroscopy of arginine in gas and solid phases. J Phys Chem B 116:12641–12650. doi:10.1021/jp302309u
168. Stolte W, Hansen D, Piancastelli M, Dominguez Lopez I, Rizvi A, Hemmers O (2001) Anionic photofragmentation of CO: a selective probe of core-level resonances. Phys Rev Lett 86 (20):4504–4507. doi:10.1103/PhysRevLett.86.4504
169. Lin Y-S, Lu K-T, Lee YT, Tseng C-M, Ni C-K, Liu C-L (2014) Near-edge X-ray absorption fine structure spectra and site-selective dissociation of phenol. J Phys Chem A 118 (9):1601–1609. doi:10.1021/jp500284r
170. Billas IM, Châtelain A, de Heer WA (1994) Magnetism from the atom to the bulk in iron, cobalt, and nickel clusters. Science 265(5179):1682–1684. doi:10.1126/science.265.5179.1682
171. Krückeberg S, Beiersdorfer P, Dietrich G, Lützenkirchen K, Schweikhard L, Walther C (1997) First observation of multiply charged vanadium clusters in a Penning trap. Rapid Commun Mass Spectrom 11(5):455–458
172. Terasaki A, Majima T, Kondow T (2007) Photon-trap spectroscopy of mass-selected ions in an ion trap: optical absorption and magneto-optical effects. J Chem Phys 127(23):231101. doi:10.1063/1.2822022
173. Majima T, Terasaki A, Kondow T (2008) Optical pumping by a laser pulse traveling in a cavity. Phys Rev A 77(3):033417. doi:10.1103/PhysRevA.77.033417
174. Terasaki A, Majima T, Kasai C, Kondow T (2009) Photon-trap spectroscopy of size-selected free cluster ions: “direct” measurement of optical absorption of Ag+ 9. Eur Phys J D 52 (1–3):43–46. doi:10.1140/epjd/e2008-00274-0

175. Egashira K, Bartels C, Kondow T, Terasaki A (2011) Optical absorption spectrum of the silver dimer ion: temperature dependence measured by photodissociation and photon-trap spectroscopy. Eur Phys J D 63(2):183–187. doi:10.1140/epjd/e2011-10525-6
176. Hirsch K, Zamudio-Bayer V, Rittmann J, Langenberg A, Vogel M, Möller T et al (2012) Initial- and final-state effects on screening and branching ratio in 2p x-ray absorption of size-selected free 3d transition metal clusters. Phys Rev B 86(16):165402. doi:10.1103/PhysRevB.86.165402
177. Lau JT, Vogel M, Langenberg A, Hirsch K, Rittmann J, Zamudio-Bayer V et al (2011) Communication: highest occupied molecular orbital-lowest unoccupied molecular orbital gaps of doped silicon clusters from core level spectroscopy. J Chem Phys 134(4):41102. doi:10.1063/1.3547699
178. Vogel M, Kasigkeit C, Hirsch K, Langenberg A, Rittmann J, Zamudio-Bayer V et al (2012) 2p core-level binding energies of size-selected free silicon clusters: chemical shifts and cluster structure. Phys Rev B 85(19):195454. doi:10.1103/PhysRevB.85.195454
179. Hirsch K, Zamudio-Bayer V, Ameseder F, Langenberg A, Rittmann J, Vogel M et al (2012) 2p x-ray absorption of free transition-metal cations across the 3d transition elements: calcium through copper. Phys Rev A 85(6):062501. doi:10.1103/PhysRevA.85.062501
180. Niemeyer M, Hirsch K, Zamudio-Bayer V, Langenberg A, Vogel M, Kossick M et al (2012) Spin coupling and orbital angular momentum quenching in free iron clusters. Phys Rev Lett 108(5):057201. doi:10.1103/PhysRevLett.108.057201
181. Zamudio-Bayer V, Leppert L, Hirsch K, Langenberg A, Rittmann J, Kossick M et al (2013) Coordination-driven magnetic-to-nonmagnetic transition in manganese-doped silicon clusters. Phys Rev B 88(11):115425. doi:10.1103/PhysRevB.88.115425
182. Langenberg A, Hirsch K, Ławicki A, Zamudio-Bayer V, Niemeyer M, Chmiela P et al (2014) Spin and orbital magnetic moments of size-selected iron, cobalt, and nickel clusters. Phys Rev B 90(18):184420. doi:10.1103/PhysRevB.90.184420
183. Daly S, Krstic M, Giuliani A, Antoine R, Nahon L, Zavras A, et al. (2015) Gas-phase VUV photoionization and photofragmentation of the silver deuteride nanocluster [Ag10D8L6]2+ (L=bis(diphenylphosphino)methane). A joint experimental and theoretical study. Phys Chem Chem Phys 17(39):25772–25777. doi:10.1039/c5cp01160d
184. Burda C, Chen XB, Narayanan R, El-Sayed MA (2005) Chemistry and properties of nanocrystals of different shapes. Chem Rev 105(4):1025–1102. doi:10.1021/cr030063a
185. Schliehe C, Schliehe C, Thiry M, Tromsdorf UI, Hentschel J, Weller H, Groettrup M (2011) Microencapsulation of inorganic nanocrystals into PLGA microsphere vaccines enables their intracellular localization in dendritic cells by electron and fluorescence microscopy. J Control Release 151(3):278–285. doi:10.1016/j.jconrel.2011.01.005
186. Flagan RC, Lunden MM (1995) Particle structure control in nanoparticle synthesis from the vapor phase. Mater Sci Eng A 204(1–2):113–124
187. Sublemontier O, Kintz H, Lacour F, Paquez X, Maurice V, Leconte Y et al (2011) Synthesis and on-line size control of silicon quantum dots. Kona Powder Part J 29:236–250
188. Ravagnan L, Mazza T, Bongiorno G, Devetta M, Amati M, Milani P et al (2011) sp hybridization in free carbon nanoparticles–presence and stability observed by near edge X-ray absorption fine structure spectroscopy. Chem Commun (Camb) 47(10):2952–2954
189. Ravagnan L, Bongiorno G, Bandiera D, Salis E, Piseri P, Milani P et al (2006) Quantitative evaluation of sp/sp(2) hybridization ratio in cluster-assembled carbon films by in situ near edge X-ray absorption fine structure spectroscopy. Carbon 44(8):1518–1524. doi:10.1016/j.carbon.2005.12.015
190. Diaz J, Monteiro OR, Hussain Z (2007) Structure of amorphous carbon from near-edge and extended x-ray absorption spectroscopy. Phys Rev B 76(9):094201. doi:10.1103/PhysRevB.76.094201
191. Kasrai M, Brown JR, Bancroft GM, Yin Z, Tan KH (1996) Sulphur characterization in coal from X-ray absorption near edge spectroscopy. Int J Coal Geol 32(1–4):107–135. doi:10.1016/S0166-5162(96)00033-X

192. Sutherland DGJ, Kasrai M, Bancroft GM, Liu ZF, Tan KH (1993) Si L-edge and K-edge X-ray-absorption near-edge spectroscopy of gas-phase Si(CH3)(x)(OCH3)(4-X) – models for solid-state analogs. Phys Rev B 48(20):14989–15001. doi:10.1103/PhysRevB.48.14989
193. Bresch H (2007) Doctoral thesis. Freie Universität Berlin
194. Garcia B, Salome M, Lemelle L, Bridot JL, Gillet P, Perriat P et al (2005) Sulfur K-edge XANES study of dihydrolipoic acid capped gold nanoparticles: dihydrolipoic acid is bound by both sulfur ends. Chem Commun 3:369–371. doi:10.1039/b411231h
195. Roux S, Garcia B, Bridot JL, Salome M, Marquette C, Lemelle L et al (2005) Synthesis, characterization of dihydrolipoic acid capped gold nanoparticles, and functionalization by the electroluminescent luminol. Langmuir 21(6):2526–2536. doi:10.1021/la048082i
196. Dezarnaud C, Tronc M, Hitchcock AP (1990) Inner shell spectroscopy of the carbon—sulfur bond. Chem Phys 142(3):455–462
197. Mei BC, Susumu K, Medintz IL, Delehanty JB, Mountziaris TJ, Mattoussi H (2008) Modular poly(ethylene glycol) ligands for biocompatible semiconductor and gold nanocrystals with extended pH and ionic stability. J Mater Chem 18(41):4949–4958. doi:10.1039/b810488c
198. Volkert AA, Subramaniam V, Ivanov MR, Goodman AM, Haes AJ (2011) Salt-mediated self-assembly of thioctic acid on gold nanoparticles. ACS Nano 5(6):4570–4580. doi:10.1021/nn200276a
199. Kravis SD, Church DA, Johnson BM, Levin JC, Azuma Y, Sellin IA et al (1991) Sequential photoionization of ions using synchrotron radiation and a Penning ion trap. Nucl Instrum Methods Phys Res Sect B 56–57:396–399. doi:10.1016/0168-583X(91)96056-Q
200. West JB (2001) Photoionization of atomic ions. J Phys B Atomic Mol Phys 34(18):R45–R91
201. Gokhberg K, Kolorenč P, Kuleff AI, Cederbaum LS (2014) Site- and energy-selective slow-electron production through intermolecular Coulombic decay. Nature 505(7485):661–663. doi:10.1038/nature12936
202. Zubavichus Y, Shaporenko A, Grunze M, Zharnikov M (2009) NEXAFS spectroscopy of biological molecules: from amino acids to functional proteins. Nucl Instrum Methods Phys Res Sect A 603(1–2):111–114. doi:10.1016/j.nima.2008.12.171
203. Messer BM, Cappa CD, Smith JD, Wilson KR, Gilles MK, Cohen RC, Saykally RJ (2005) pH dependence of the electronic structure of glycine. J Phys Chem B 109(11):5375–5382. doi:10.1021/jp0457592
204. Nolting D, Aziz EF, Ottosson N, Faubel M, Hertel IV, Winter B (2007) pH-induced protonation of lysine in aqueous solution causes chemical shifts in X-ray photoelectron spectroscopy. J Am Chem Soc 129(45):14068–14073. doi:10.1021/ja0729711
205. Ottosson N, Børve KJ, Spångberg D, Bergersen H, Sæthre LJ, Faubel M et al (2011) On the origins of core-electron chemical shifts of small biomolecules in aqueous solution: insights from photoemission and ab initio calculations of glycine(aq). J Am Chem Soc 133 (9):3120–3130. doi:10.1021/ja110321q
206. Fronzoni G, Baseggio O, Stener M, Hua W, Tian G, Luo Y et al (2014) Vibrationally resolved high-resolution NEXAFS and XPS spectra of phenanthrene and coronene. J Chem Phys 141:044313. doi:10.1063/1.4891221
207. Reitsma G, Boschman L, Deuzeman MJ, González-Magaña O, Hoekstra S, Cazaux S et al (2014) Deexcitation dynamics of superhydrogenated polycyclic aromatic hydrocarbon cations after soft-x-ray absorption. Phys Rev Lett 113(5):053002. doi:10.1103/PhysRevLett.113.053002
208. Winter B (2009) Liquid microjet for photoelectron spectroscopy. Nucl Instrum Methods Phys Res Sect A 601(1–2):139–150. doi:10.1016/j.nima.2008.12.108
209. Faubel M, Siefermann KR, Liu Y, Abel B (2012) Ultrafast soft X-ray photoelectron spectroscopy at liquid water microjets. Acc Chem Res 45(1):120–130
210. Brown MA, Jordan I, Beloqui Redondo A, Kleibert A, Wörner HJ, Van Bokhoven JA (2013) In situ photoelectron spectroscopy at the liquid/nanoparticle interface. Surf Sci 610:1–6. doi:10.1016/j.susc.2013.01.012

211. Brown MA, Redondo AB, Jordan I, Duyckaerts N, Lee MT, Ammann M et al (2013) A new endstation at the Swiss Light Source for ultraviolet photoelectron spectroscopy, X-ray photoelectron spectroscopy, and X-ray absorption spectroscopy measurements of liquid solutions. Rev Sci Instrum 84(7):073904
212. Winter B, Faubel M (2006) Photoemission from liquid aqueous solutions. Chem Rev 106 (4):1176–1211
213. Bergersen H, Marinho RRT, Pokapanich W, Lindblad A, Björneholm O, Sæthre LJ, Öhrwall G (2007) A photoelectron spectroscopic study of aqueous tetrabutylammonium iodide. J Phys Condens Matter 19(32):326101